QUANTIFYING DIFFERENCES IN CT IMAGE QUALITY BETWEEN A MODEL-BASED ITERATIVE RECONSTRUCTION ALGORITHM, AN ADAPTIVE ITERATIVE RECONSTRUCTION ALGORITHM, AND FILTERED BACKPROJECTION

By

Hayley M. Whitson

A THESIS

Presented to the Department of Medical Physics

and the Oregon Health & Science University

School of Medicine

in partial fulfillment, of

the requirements for the degree of

Master of Science

June 2017

School of Medicine

Oregon Health & Science University

CERTIFICATE OF APPROVAL

This is to certify that the Master's thesis of

Hayley M. Whitson

has been approved

Mentor/Advisor

Member

Member

TABLE OF CONTENTS

LIST OF FIGURES

ACKNOWLEDGMENTS

I would first and foremost like to thank my advisors Dr. Thomas Griglock and Dr. Lindsay DeWeese. Your patience and commitment to my fellow students and me provided us with countless opportunities to learn skills in the clinic, when conducting research, and, most importantly, in the communication of ideas. This guidance has fostered my drive for clinically applicable research and a major appreciation for medical imaging. Dr. Griglock, thank you for your constant encouragement, steadfast support, and quick-reply e-mail skills. This project would not have come to fruition without you.

A very special thanks to Kirsten Boedeker from Toshiba Medical Systems for spending a day out of your vacation time to help me with my MATLAB code for the modulation transfer function, I am forever grateful. And thank you to Erin Angel from Toshiba Medical Systems for your guidance and for spending weeks reconstructing the raw data with FIRST for us. Thank you to Nathan Skidmore for helping with the reconstructions.

I would like to thank all of the OHSU Medical Physics Program professors for your time and wisdom. To Dr. Rick Crilly, thank you for recognizing the look of hopelessness on my face and spending a few hours helping me understand the modulation transfer function. I don't think I would have cracked it without your viewpoint! I would also like to thank Chelsea Page and Travis Bryant for holding me up in so many ways. And to Isaac Bailey for not leaving me alone in the diagnostic imaging track! I am glad

we all experienced this program together. To Celeste and Dylan, thank you for your help with programming and for playing board games with me!

I want to express the most gratitude to my family. Mom, you have been the best role model of resilience and I love you for your unwavering support. Grandma, your laughter and care for others is a constant positive influence, thank you for always being one of many inspiring women in our family. Siblings, you get it, I love you all very much. And to the many aunts, uncles, cousins, and extending-family thank you! And, of course, to you dad, I love and miss you so much. When I finish that PhD dissertation, it will be dedicated to you.

I must thank my friends, especially my Portland fam, new and old, for your support over the last two years. It was not easy an easy road for me, and the silliness, dancing, board games, concerts, potlucks, and just overall caring that ensued was essential to completing this project. I love you all so much, looking forward to many more years of friendship.

In closing, I would like to dedicate this work to my island hometown of Sitka, Alaska. We have lost too many good souls over the years. But watching the town come together to hold each other up and to support the families of those lost is an inspiration. Although there are others, for me, the thoughts of Joe Whitson, Duane Whitson, Michael Abt, Ryan Staton, Ulisses Diaz, Elmer Diaz, my dog Fathom, Joe Mettler, and Ali Clayton conjure such good memories and laughter. You each taught me strength and love, I miss you all. We are Sitka strong.

ABSTRACT

BACKGROUND

To inform and advocate for clinical implementation of model-based iterative reconstruction (MBIR) techniques for computed tomography (CT), the complex relationships between spatial resolution, noise, and dose index must be explored and quantified. This study aimed to provide data illustrating which clinical applications may be gained from implementing MBIR by comparing metrics with commonly used reconstruction algorithms (adaptive IR and filtered back-projection).

METHODS

Comparisons were performed using images of the American College of Radiology CT accreditation phantom. The phantom was scanned on a Toshiba Aquilion One ViSON CT scanner at five tube currents: 45, 90, 180, 270, and 350 mA corresponding to $CTDI_{vol}$ levels of 2.5, 5, 10, 14.9, and 19.4 respectively. Each data set was reconstructed with four reconstruction algorithms: filtered backprojection (FBP) and three iterative techniques by Toshiba Medical Systems (AIDR 3D, FIRST Body and FIRST Body Sharp). To compare measurements from images with more realistic patient dimensions, the phantom was also scanned with an attenuation body ring. The CT number accuracy, noise-power spectrum, and task-based modulation transfer function were calculated for each dose index and reconstruction combination using a self-written MATLAB analysis program.

RESULTS

Reconstruction algorithm dependence was seen for all image quality metrics. Overall, the FIRST algorithms provided more consistent CT numbers with differing dose indices although filtered backprojection and AIDR 3D were more accurate for lower contrast inserts and water at lower doses. Noise in the CT accuracy measurements was reduced at a minimum of 28% using FIRST (from filtered backprojection) and ranged up to an 81% reduction. At low doses, the magnitude of the noise power spectrum of FIRST Body is around half that of filtered backprojection. The use of the attenuation ring showed FIRST more capable of balancing noise through thicker attenuation layers. Furthermore, the peak frequencies of the noise power spectrum were much lower for FIRST, suggesting filtered backprojection and AIDR 3D have more noise at smaller object sizes. As expected, FIRST showed a dependence on contrast level and dose index for spatial resolution whereas FBP stayed steady across all inserts and tube currents. In almost all circumstances, the limiting spatial frequency of FIRST is much larger than the other algorithms, showing that smaller objects can be resolved. However, at lower tube currents, FBP and AIDR 3D performed better for low contrast materials such as polyethylene and acrylic. With use of the attenuation ring, the spatial resolution of FIRST was more dramatically reduced than FBP, however, the limiting spatial resolution of FIRST was still well above that of FBP.

CONCLUSIONS

The FIRST algorithm shows promise in maintaining image quality while reducing radiation dose levels, especially if optimized for specific clinical applications. MBIR has so far experienced difficulties transitioning into clinical use. The inherent complexities of MBIR necessitate the need for more studies in order to fully understand the clinical potential of these algorithms and to provide robust reasoning for their application. The findings of studies such as this one can provide information on balancing various image characteristics for optimal clinical applications and patient care for MBIR CT.

1 INTRODUCTION

Computed tomography (CT), an imaging modality highly used in today's clinical setting, was first actualized in the early 1970s[1]. Since then, modern technological advancements have accelerated CT's use and applications[2]. In fact, according to IMV's *2016 CT Market Outlook Report*, 82 million CT procedures were performed in the U.S. in 2016, a 4% increase from 2015[3]. This increase in the number of CT exams also results in an increase in radiation exposure to patients.

The fear of increased exposure is due to the possibility of radiation-induced DNA damage leading to genetic mutations and potentially to cancer[1]. This fear is more substantiated at high radiation doses and energies such as those found in radiation therapy or radiation disasters[1,4,5]. At diagnostic exposure levels, such as those in a CT examination, the definitive induction of a cancer is uncertain due to the complicated interplay of latency periods, age of the patient during exposure, gender of the patient, genetic effects, and other confounding factors[1,5]. In addition, because low doses are a relatively weak carcinogen, the population sizes needed to perform an accurate study would be extremely large[4,5]. Nevertheless, the radiological community assumes there is a non-zero risk at diagnostic exposure levels, motivating the use of dose reduction techniques[4,5].

Although the individual risk of radiation-induced cancer may be small, if one considers the large portion of the population being exposed, they may see the potential concern for public health in the future[5]. In addition, low-dose CT has recently been implemented for screening cigarette smokers for lung cancer[6]. CT screening has also

been suggested for detection of cardiac disease and colon polyps[5]. These types of screening programs will further increase the overall population exposure to CT[5]. Due to the uncertainty in cancer risk and health concerns of widespread exposure, a major focus of CT research is driven by exposure reduction.

The reduction of radiation exposure can be achieved through many different means. A new and promising method to achieve this reduction is through iterative reconstruction (IR) techniques. By changing the processing workflow of collected CT data, images with equivalent diagnostic performance can be generated with reduced exposure for the patient[7–9]. Thus far, statistical IR techniques have been adopted into clinical practice[7]. However, further advancements have now led to the development of model-based iterative reconstruction (MBIR) algorithms[7]. MBIR algorithms show promise in further dose reduction potential with maintained image quality but have not yet been widely implemented clinically[7,10–13]. Additional understanding of the image properties of MBIR is necessary to fully discern both why and how it should be clinically implemented.

In this work, the performance of a new model-based iterative reconstruction algorithm (FIRST, Toshiba Medical Systems) was assessed through image quality comparisons with currently used clinical reconstruction algorithms. The goal of the project was to perform robust quantification of the relationships between image quality and various dose levels. This quantified description is necessary to inform clinical implementation of FIRST.

2 BACKGROUND

2.1 COMPUTED TOMOGRAPHY UTILITY

CT is used to image anatomy ranging from the brain, to the torso, and to the extremities, yielding widespread use and immense applicability in the clinic. Due to technological advances, such as helical and multidetector CT, the diagnostic power and consequently the number of CT imaging studies has greatly increased over time[8]. In addition to providing improved image quality, hardware upgrades also increased acquisition speed which in turn increased the potential patient volume, adding to the growing number of exams[1]. As a result of these innovations, the use of CT has increased at a rate of ~10 to 11% annually from 1993 to 2006[2].

A major reason for this growth is due to the ability of CT to provide physicians with images of the patient in any anatomical plane. For most acquisitions, computed tomography collects data from a full 360-degree rotation of an x-ray tube around the patient. This data is then computationally reconstructed into a virtual stack of image slices comprised of three-dimensional volume elements, also called voxels, which contain information analogous to the patient's anatomy.

2.2 COMPUTED TOMOGRAPHY IMAGE RECONSTRUCTION

At its most basic level, during a CT exam the x-ray tube and detector rotate around the patient, and millions of measurements are recorded. These measurements represent the amount of x-ray energy that was transmitted through the patient and, inversely, the

amount of attenuation along the beam's path. X-ray attenuation occurs exponentially per the equation,

$$I = I_0 e^{-\int \mu(x,y,z)ds} \tag{1}$$

where $\mu(x, y, z)$ is the attenuation factor at a given location within the patient along the beam path, s[1]. Thus, the forward projection, p, of the beam at a specific angle, θ, is the line integral of the attenuation coefficients along the path[1],

$$p(\theta) = \ln\left(\frac{I}{I_0}\right) = -\int \mu(x, y, z)ds \tag{2}$$

The goal of CT reconstruction is to solve the system of equations from all projections collected from $\theta = 0$ to $360°$ in order to assign an attenuation factor to each specific voxel. These attenuation factors are then converted into the more useful Hounsfield units defined by

$$HU(x, y, z) = 1000 * \frac{\mu(x, y, z) - \mu_w}{\mu_w} \tag{3}$$

where μ_w is the linear attenuation coefficient of water. Due to the fact that Hounsfield units have direct correlation to tissue attenuation, CT data is inherently quantitative, adding it its utility.

To produce an image from the raw projections, the data is processed with mathematical formulations, also known as reconstruction algorithms. These processes reconstruct the data into a visual representation of anatomical structures, which are then used for diagnosis. Two forms of reconstruction algorithms are filtered backprojection and iterative reconstruction.

2.2.1 FILTERED BACKPROJECTION

Backprojection of the system of linear equations found from Equation (2) is performed through an inversion process[8]. By projecting the measured data back onto the image matrix, the overlapping data from each projection angle adds information to each voxel[1]. With all the collected projections, an image of the original object can be formulated onto the matrix[1]. However, due to the nature of combining many angles, a characteristic $\frac{1}{r}$ blurring occurs[1]. This is typically corrected for with a mathematical filter, sometimes referred to as a convolution[1]. In the case of filtering the backprojection blur, a deconvolution process is used. This mathematical filter can be defined as,

$$p'(x) = p(x) \oplus h(x) = \int_{x'=-\infty}^{\infty} p(x) * h(x - x')dx' \tag{4}$$

where $p(x)$ is the original projection, $h(x)$ is the deconvolution kernel, and $p'(x)$ is the corrected projection[1]. In effect, this deconvolution process removes the artificial blurring and faithfully represents the imaged object. It is this mathematical operand that gives filtered backprojection (FBP) its name[1].

Due to the time constraints of medical imaging, using a Fourier transform method can decrease reconstruction times[1]. The Fourier transform is applied to Equation (4) to produce an equivalent effect,

$$p'(x) = \text{FT}^{-1}\{\, \text{FT}[p(x)] * \text{FT}[h(x)] \,\} \tag{5}$$

where FT[] is the Fourier transform and FT^{-1} is the inverse Fourier transform[1]. The Fourier transform of the deconvolution kernel is sometimes referred to as the ramp filter which has a characteristic $\frac{1}{f}$ shape in the frequency domain[1]. However, this shape

preferentially amplifies the high spatial frequency components of the image[1]. Image noise, discussed in more detail in Section 2.3.2, typically occurs in this frequency range[1]. Thus, in practice, a roll off function is used in place of the ramp filter to reduce the amplification of noise[1]. The amount of roll-off applied in the ramp filter is chosen based on the clinical application[1]. This is because increased roll-off reduces noise, however, it also reduces the amount of blur reduction and hence reduces spatial resolution[1]. This tradeoff can be balanced for clinical need with both dose and exam indication.

Filtered backprojection was the standard reconstruction algorithm for CT imaging for many years. Now, due to modern computing power increases, iterative reconstruction techniques are a tangible solution to preserve image quality with reduced dose[7,8].

2.2.2 ITERATIVE RECONSTRUCTION TECHNIQUES

Until recently, the evolution of CT technology has mostly been driven by advances in hardware including spiral CT, multidetector CT, and dual-source CT[8]. However, due to advancements in computing power, other realms of development are becoming important. One notable area in CT growth is innovations in reconstruction algorithms. With improved computer capacities, more complex reconstruction algorithms such as iterative reconstruction (IR) techniques can be used without sacrificing computing time[8].

As opposed to filtered backprojection which uses simple mathematical assumptions, IR techniques utilize statistical models, geometric models, or both, in order to employ a cycle of updating information which improves CT diagnostic performance[7]. This cycle essentially turns the reconstruction problem into one of optimization[14].

Simplistically, the process can be broken into four steps. First, what is known as a seed image, or estimation image, is constructed. This seed image is then compared with the measured data to identify differences between the two. Thirdly, these determined differences are corrected by the algorithm which, depending on the manufacturer, includes varying models of the CT scanner and x-ray spectrum. This modeled information aids in determining a more accurate attenuation value for each voxel. Fourth, steps two and three are repeated iteratively until the differences between the two images meet a preset requirement. Once this requirement is met, the cycle is terminated providing the final image. The degree to which geometric and statistical information are included in the reconstruction process determines which type of iterative reconstruction is being performed. Two important types of iterative reconstruction are statistical IR and model-based IR which are discussed in the following two sections.

2.2.2.1 STATISTIAL ITERATIVE RECONSTRUCTION: AIDR 3D

Sometimes also called hybrid algorithms, statistical iterative algorithms are a mixture of traditional algebraic algorithms such as filtered backprojection as well as iterative techniques[8]. Usually focusing solely on noise reduction, adaptive algorithms are not extremely time consuming and are clinically used on scanners today[7]. In this research, an adaptive algorithm, Adaptive Iterative Dose Reduction 3D (AIDR 3D, Toshiba Medical Systems), was utilized.

Statistical, anatomical, and scanner models are all included in AIDR 3D's iterative reconstruction optimization which focuses on reducing noise while preserving spatial resolution[15]. The statistical portion of the model considers statistical fluctuations

in photon counting while the anatomical and scanner models provide a more accurate description of noise in projection space[16]. Iterations are performed in both the raw image data domain and the reconstruction domain[8]. A FBP image is blended with the iteratively constructed image to maintain image noise properties consistent with those usually seen in FBP images, thus allowing easier clinical implementation due to radiologists' familiarity with this noise texture[15]. AIDR 3D has proven itself to be clinically adaptive and useful. Further advancements in the field have now lead to the formulation of model-based iterative reconstruction techniques.

2.2.2.2 MODEL-BASED ITERATIVE RECONSTRUCTION: FIRST

Typically more complex than statistical iterative reconstruction methods, model-based iterative reconstruction (MBIR) techniques attempt to model the process of acquiring CT images as thoroughly as possible[16]. This usually includes geometric modeling of the CT scanner and detector, statistical modeling of photons, and noise regularization[16]. Several studies have shown MBIR to be superior to FBP and statistical IR in terms of reduced radiation dose with preserved image quality metrics[7,8,10,14,17–19]. It is this dose reduction potential that fuels the need to understand these new algorithms thoroughly.

As the main subject of inquiry for this study is the MBIR algorithm FIRST (Toshiba Medical Systems), the following description only concerns the specifics of FIRST. Other MBIR algorithms may have differences in their reconstruction process. Forward-projected model-based Iterative Reconstruction SoluTion (FIRST) is a newly developed algorithm that is not yet widely implemented clinically. Its process starts with

a rough FBP reconstruction called the seed image[20]. The seed image is next mathematically forward projected based on known qualities of the image acquisition process[20]. This creates a synthesized forward projected estimation of the true image[20]. This synthesized image is then mathematically compared with the raw measured data producing a library of differences between the forward projected data and the raw data[20]. These differences provide information on components of the image which could be improved[20]. A correction is thus calculated to update the forward projected image[20]. The corrected image is produced through backprojecting these corrections onto image space[20]. This updated version is then compared to the original projection data once again[20]. This cycle repeats iteratively until a predetermined accepted difference value is achieved, no correction is needed, and the final image is stored[20].

Mathematically, the MBIR process can be described by the objective function,

$$\hat{x} = \arg min_{x \geq 0} \frac{1}{2} \|y - Ax\|_w^2 + \beta R(x) \tag{6}$$

where the left-hand term is called the data fidelity term, which is minimized during the process, and the right-hand term is the regularization term, necessary to ensure a reduction in noise[20]. Specifically, A is a linear operator, y is the measured data, x is the synthesized data, and β is a parameter[20]. Accurate modeling of the CT system is necessary for minimizing the data fidelity term which provides FIRST images with improved spatial resolution[20]. The regularization function for FIRST incudes both statistical edge-preserving noise reduction and anatomically-based noise reduction functions[20].

FIRST uses four models of the imaging system: statistical noise, CT scanner, optics, and cone beam[20]. The statistical noise model includes information about photon

statistics, anatomical noise, structural noise, and electronic noise[20]. Forward projections require an extremely accurate model of the scanner, thus FIRST incorporates models of the CT scanner geometry including bowtie filtration, collimation, source to isocenter, and detector geometry[20]. This greatly differs from FBP reconstructions in which the detector elements and focal spot size are considered to be infinitesimally small[16]. Both modeling the focal spot and detector elements as three dimensional and including information on detector material absorption factors improves spatial resolution of the resulting images[16]. Traditional reconstruction algorithms simply model the x-ray spectrum as monoenergetic[16]. This is inherently unrealistic and thus the polyenergetic nature of the beam is modeled into the MBIR algorithm's optics model[16]. The optics model describes the x-ray spectrum, its path, and random variations in each individual photon's path[20]. In addition, energy dependent scatter and beam-hardening effects are also included[16]. The optics model helps to reduce artifacts such as cupping and streaking around high-Z materials[16]. And lastly, the cone beam model reduces the amount of artifact from the wide cone angle of the beam[20]. Each of these models contributes to calculating image corrections during each iteration[20].

The FIRST algorithm has six settings: Cardiac, Cardiac Sharp, Bone, Body, and Body Sharp. Each setting provides optimization for specific anatomical fluctuations. In this research, FIRST Body and FIRST Body Sharp were analyzed. These settings are meant to be used when imaging the abdomen and pelvis.

Despite the improvements in image quality and the dose reduction potential, MBIR algorithms have been historically difficult to implement in the clinic[7]. The noise reduction algorithms can cause the images to have a different, often unnatural, image

texture[7]. This may require adaptation by the radiologic community in order for MBIR images to be clinically successful[7].

2.3 IMAGE QUALITY IN CT

There are multiple metrics which assess CT image quality. These metrics provide a way to compare reconstruction algorithms. In these comparisons, it is advantageous to replicate clinical situations by varying the dose and phantom size.

In this study, the image quality metrics of CT number accuracy, noise, and high-contrast spatial resolution were evaluated for three reconstruction algorithms. A description of each of these metrics is described in the following sections. In addition, special considerations must be taken when measuring image quality on IR techniques, this is discussed first.

2.3.1 RECONSTRUCTION ALGORITHM DEPENDENCE

It is important to note that the reconstruction algorithm used to create an image influences image quality measurements. This is true even when comparing different roll off functions, also called filters, in filtered backprojection[1]. As described in Section 2.2.1, the amount of roll off can reduce noise, but it influences spatial resolution. It is thus important the same filter is used across reconstruction algorithms if they are to be compared.

Furthermore, when iterative reconstruction techniques are used, traditional metrics of image quality must be scrutinized[1,21]. This is because measurements of the modulation transfer function (MTF, Section 2.3.4.2) and noise power spectrum (NPS,

Section 2.3.3.2) require that the system is linear in nature[1,22]. In loose terms, filtered backprojection can be assumed to be linear[1]. However, IR has been shown to be non-linear due to the nature of iteration[1,21]. In other words, the point spread function of the system is not the same in all locations; it is non-stationary[1]. Due to this, the MTF and NPS become highly dependent on the contrast levels within the image as well as the location of measurement for IR techniques[1,21].

Departing from the characteristics of FBP, and due to the non-linearity, the spatial resolution of MBIR is both dose and contrast dependent, described in more detail in Section 2.3.4.3[21,23]. Noise and spatial resolution are also highly dependent on one another, making patient size an important factor as well[23]. These aspects result in a much more complicated process for protocol optimization in the clinic for MBIR and a necessity for more studies such as this one to understand this complicated interplay[23,24]. A more detailed description of how these effects change noise and spatial resolution measurements are discussed in their respective background sections.

2.3.2 CT NUMBER ACCURACY

As described in Section 2.2, materials within the body have differing attenuation properties which can be defined by their Hounsfield unit (Equation (3)). CT number accuracy measures how well a system portrays the HUs of a known material which is important for clinical diagnoses. Materials commonly imaged for quality control include bone equivalent, water equivalent, acrylic, air, and polyethylene. These are chosen as they mimic the electron density properties of materials found in the body.

The CT number of a given volume of interest (VOI) is the mean value of Hounsfield units (HUs) of the voxels within the VOI[25]. The standard deviation of HUs within the VOI is a measurement of spread and thus provides information on the noise within this area[25]. Noise standard deviation is described more in Section 2.3.3.1.

2.3.3 NOISE

There are a few origins of noise relevant in CT imaging: electronic noise, anatomical noise, and quantum noise[1]. Electronic noise originates from the electronics which carry the signal information through the system[1]. If electrons are added to the signal flow through un-related events such as thermal noise or shot noise, they inherently add information to the signal that is not due to events occurring inside the patient[1]. In low signal situations, such as when the dose level is low, the ratio of signal to electronic noise can be high, degrading the final image[1].

Anatomical noise is due to patient anatomy that is not important to the diagnosis[1]. An example given by Bushberg et al. is from digital subtraction angiography, a fluoroscopic study, in which injection of contrasts agents allows image subtraction of all anatomy except the vascular anatomy[1]. In CT and other tomographic modalities, overlapping anatomy is not an issue due to the three-dimensional nature of the image collection[1]. In essence, anatomical noise is greatly reduced "through spatial isolation[1]."

Statistical fluctuations in the numbers of x-ray photons is called quantum noise[1]. In x-ray imaging, photons follow a Poisson distribution[1]. The number of photons, *N*, recorded in each detector element is,

$$N = \varphi A \varepsilon \tag{7}$$

where φ is the photon fluence on the detector (photons/mm^2), A is the area of each element (mm^2), and ε is the detector efficiency[1]. Using a normal approximation of the Poisson distribution, we can then define the quantum noise as[1],

$$\sigma = \sqrt{N} \tag{8}$$

If this relationship is turned into relative noise, i.e. a percentage, we find[1],

$$\text{relative noise} = \frac{\sigma}{N} = \frac{\sqrt{N}}{N} \tag{9}$$

This relationship shows that with an increase in *N*, the relative noise in the image will decrease. Thus, by adjusting techniques on the CT scanner to increase the number of photons, the noise in the resulting image will be reduced. However, there is a linear relationship between *N* and the dose to the patient[1]. This is an important tradeoff in x-ray imaging as noise reduction aids in clinical diagnoses, but it is important to attempt to keep radiation doses low.

2.3.3.1 MEASUREMENTS OF NOISE: STANDARD DEVIATION

One way to measure the noise of an image is through measuring σ in a homogenous area of a phantom image[1]. The standard deviation, σ, is calculated using the HUs of a given VOI within the homogeneous area,

$$\sigma = \sqrt{\frac{\sum_{i=1}^{N}(HU_i - \overline{HU})^2}{N-1}} \tag{10}$$

for all voxels $i = 1$ to N within the VOI[1]. Similar to CT number accuracy, the standard deviation can be measured for differing materials within the phantom to display material dependent noise.

2.3.3.2 MEASUREMENTS OF NOISE: NOISE POWER SPECTRUM

The standard deviation of HUs within a VOI, although useful, is a simple metric for measuring noise. Two areas in the image could have an equivalent value of σ but look very different to an observer[21]. These areas are then described as having different noise textures, or a difference in the spatial-frequency distribution of noise[21].

The origin of spatially dependent noise is the correlation between adjacent detector elements[1]. Imaging systems have a blur phenomenon that occurs in the point spread function and line spread function[1]. This blurring causes the possibility of noise sharing across adjacent voxels and thus a spatially dependent noise[1]. With no blur in the system, there would be no correlation between voxels which would result in what we call white noise[1]. The noise power spectrum (NPS) is a measurement of the frequency dependent noise variance of an image[21]. In modern CT scanners, multi-detector arrays and helical imaging induce the possibility of noise correlation occurring in the *z* dimension as well as in the axial plane (*x* and *y*)[1]. Thus, it is important to calculate the 3D noise power spectrum to include all potential correlation in the image[1].

With Δ_x, Δ_y, and Δ_z denoting the pixel spacing in each dimension (mm), N_x, N_y, and N_z denoting the number of voxels in each dimension per VOI, and f_x, f_y, and f_z denoting the spatial frequencies in each dimension, the 3D NPS is calculated through,

$$\mathrm{NPS}(f_x, f_y, f_z) = \frac{1}{N}\sum_{i=1}^{N} |\mathrm{DFT}_{3\mathrm{D}}[I_i(x,y,z) - \bar{I}_i]|^2 \frac{\Delta_x \Delta_y \Delta_z}{N_x N_y N_z} \quad (11)$$

where the summation from $i = 1$ to N and multiplication by $\frac{1}{N}$ refers to averaging the NPS over N VOIs[21]. The signal from the i^{th} VOI is denoted $I_i(x,y,z)$ and $\bar{I}_i$ is the

average of the i^{th} VOI[21]. $\text{DFT}_{3\text{D}}$ is the discrete Fourier transform in three dimensional space[21]. The resulting units of the 3D NPS are HU^2mm^3.

When the NPS is calculated, a well-studied artifact typically occurs[21]. This artifact, known as "cupping," refers to the phenomena in which HUs in the center of a cylindrical object will be lower than those near the periphery, causing a low-frequency spike in the NPS[21]. To reduce the effects of this artifact, a process known as detrending is performed on the data prior to calculations[21]. To combat this artifact, either a low-order polynomial is subtracted away from the data, or image subtraction is used[21]. As image subtraction was the method chosen for this study, it is focused on here.

As shown by Dolly et al., the subtraction method is the most effective at removing low-frequency noise[26]. The method is performed by subtracting two separately acquired image data sets of the same homogeneous volume of a phantom[21]. For data sets A and B of the same volume (x, y, z), this is,

$$K(x, y, z) = I_A(x, y, z) - I_B(x, y, z) \tag{12}$$

with $K(x, y, z)$ being the resulting noise-only image, thus removing the cupping artifact[21]. This noise-only image is then placed into Equation (11),

$$\text{NPS}(f_x, f_y, f_z) = \frac{1}{N}\sum_{i=1}^{N}|\text{DFT}_{3\text{D}}[K_i(x, y, z) - \overline{K_i}]|^2 \frac{\Delta_x\Delta_y\Delta_z}{N_xN_yN_z} \tag{13}$$

to calculate the 3D NPS[21]. Graphically, a 2D NPS is typically shown for when $f_z = 0$ and has the shape of a torus in f_y and f_x (Figure 1)[21]. From this, a 1D NPS can be formulated by radially averaging the values of f_y and f_x[21].

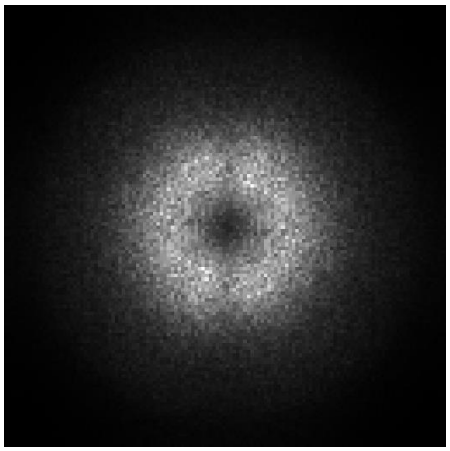

Figure 1: Example of a 2D NPS at $f_z = 0$ (FBP at 270 mA). 2D NPSs typically have the shape of a torus.

2.3.3.3 MEASUREMENTS OF NOISE: RECONSTRUCTION DEPENDENCE

The reconstruction method used can greatly affect noise in the resulting image. In filtered backprojection, because the HUs are backprojected along a line, correlated noise can exist across a long line of pixels[1]. For iterative reconstruction, the non-linearity and non-stationary statistics makes it difficult to accurately measure and characterize noise[24,26].

Especially when considering the NPS, wide-sense stationary statistics is required to properly conduct calculations[26]. As this condition does not hold in most CT acquisitions and especially not for IR, special considerations must be taken[26]. One way to approach this is to sample the image in localized volumes of interest in which stationary statistics may be approximated to be true[26]. In addition, the VOIs should be located at a constant radius from the center of the phantom and cover the full 360˚[22]. These requirements were considered in this research.

An important study by Gomez-Cardona et al. explored whether a novel power law reported by Li et al. for MBIR systems can be generalized from phantom studies to *in vivo* situations[24,27]. This power law is,

$$\sigma^2 = \alpha(\text{mAs})^{-\beta} \tag{14}$$

where σ^2 is the image noise variance, α and β are the parameters of interest, and mAs is the product of tube current and time per tube rotation (in seconds)[27]. The study utilized both an *in vivo* animal trial and a prospective human trial[27]. In the animal study, the value of β between the phantom and in vivo measurements agreed for both MBIR ($R^2 = 0.971$) and FBP ($R^2 = 0.997$)[27]. Statistical equivalency of β values with phantom measurements was also found in the human trail ($p < .05$) for both MBIR and FBP[27]. Although it is not the only important image quality measurement, these findings validate that noise variance measurements in phantoms can be translated to *in vivo* situations for MBIR, also showing promise for other image quality metrics to do the same.

2.3.4 SPATIAL RESOLUTION

The spatial resolution of an imaging system determines the ability of the system to distinguish two adjacent objects as being separate from each other[1]. This is typically split into high-contrast spatial resolution and low-contrast spatial resolution[1]. Low-contrast resolution refers to detecting small changes in signal intensity between objects whereas high-contrast spatial resolution refers to faithfully resolving the physical size of objects[1]. This work focuses on high-contrast spatial resolution for reasons described in Section 2.3.4.3. Thus, the term spatial resolution from here on refers to high-contrast spatial resolution.

2.3.4.1 MEASUREMENTS OF RESOLUTION: LINE PAIR PHANTOMS

The most idealistic method to measure the resolution of an imaging system is the point spread function (PSF)[1]. If a point source is imaged by the system, the measured signal by the system is the PSF[1]. Due to the imperfect nature of imaging, the PSF will have some blur associated with it[1]. In other words, the PSF, which theoretically should have a delta function output, will be measured as a function similar to a two-dimensional Gaussian[1].

Another method is to instead use the line spread function (LSF), or measure a slit with the imaging system[1]. The LSF and PSF are related by the equation,

$$LSF(x) = \int_{y=-\infty}^{\infty} PSF(x, y)dy \tag{15}$$

The edge spread function (ESF) is similar to the LSF except that instead of using a slit this method measures the response of the system to a sharp edge between two materials[1]. The LSF is the derivative of the ESF[1],

$$LSF(x) = \frac{d}{dx} ESF(x) \tag{16}$$

This becomes important in the measurement of spatial resolution as a sharp edge is easier to manufacture than slit or point source phantoms[1].

Historically, spatial resolution has been measured using line pair phantoms for both radiography and subsequently in CT[1]. These phantoms essentially mimic a line spread function with bars constructed of high HU materials spaced at differing frequencies[1]. Although this gives an adequate measurement of spatial resolution for routine quality control checks, a more robust measurement of spatial resolution is the modulation transfer function (MTF)[1].

2.3.4.2 MEASUREMENTS OF RESOLUTION: MODULATION TRANSFER FUNCTION

The MTF is the measurement of how contrast is transferred through the system at different object spatial frequencies[1]. If two objects are spaced far apart, their contrasts will not blur together[1]. But as objects become closer, the resulting image may share pixels and thus the contrast between the objects is lost[1]. The LSF and ESF (Equations (15) and (16)) are metrics in the spatial domain[21]. However, like the NPS for noise, it is sometimes helpful to define the system in terms of the frequency domain[21]. This is done in calculations of the MTF,

$$\mathrm{MTF}(f_x) = \frac{\left|\int_{-\infty}^{\infty} \mathrm{LSF}(x) e^{-2\pi i f_x x} dx\right|}{\int_{-\infty}^{\infty} \mathrm{LSF}(x) dx} \tag{17}$$

where f_x represents the spatial frequency in the x dimension, multiplication by the exponential is the Fourier transform, the brackets take the modulus, and the denominator normalizes the MTF to unity at $f_x = 0$ [21].

A perfect optical system would have the value of unity at all spatial frequencies, or, in other words, 100% contrast transfer. But as systems are imperfect, the MTF will eventually reach a limiting contrast transfer that can be resolved by the system[1]. This is usually quoted at the spatial frequency in which the MTF crosses the 10% level[1].

2.3.4.3 MEASUREMENTS OF RESOLUTION: RECONSTRUCTION DEPENDENCE

There are many factors affecting the spatial resolution of the system including the focal spot size, gantry motion, detector width, and sampling[1]. However, a major factor in the appearance of detail is due to the reconstruction filter chosen[1]. This is because the

amount of roll-off used to reduce noise in the image directly affects the spatial resolution[1]. Thus, when making comparisons of reconstruction algorithms, a consistent filter must be utilized.

In addition, a requirement for measuring the MTF is both a linear and shift-invariant system[22,28]. This means the PSF is consistent when measured in all locations in the image[28]. Iterative reconstruction techniques inherently break both requirements[28]. It has been shown that measurements of the MTF for IR techniques show a dependence on location and contrast (HU) level of the material forming the edge[21]. It is still possible to make valid MTF measurements on IR images by using specific conditions such as localized measurements and low contrast objects[22,28]. A technique developed by Richard et al. is to measure the MTF for differing tasks, i.e. differing contrast levels within the image, for non-linear algorithms[28]. This results in a different curve for each contrast level measured thus satisfying the characterization of the entire system[28,29]. However, it is important to keep in mind the measurements constraints when interpreting the results[22].

This research focuses only on high-contrast spatial resolution. Studies have shown traditional metrics of low-contrast resolution, such as the contrast-to-noise ratio, may not be valid metrics for IR methods[30]. Time-intensive observer studies are necessary until proper methodologies can be formulated for the measurement of low-contrast resolution in IR[30]. As such, these studies are beyond the scope of this work.

3 MATERIALS AND METHODS

3.1 CT SCAN PARAMETERS, PHANTOM SETUP, AND RECONSTRUCTIONS

All CT scans were performed on an Aquilion ONE ViSION CT system (Toshiba Medical Systems). The ACR CT accreditation phantom (Gammex, Model 464) was centered on the table using the Aquilion's laser system and scout images. To make comparisons with images with more realistic patient dimensions, the phantom was scanned both with and without a tissue-equivalent body ring (The Phantom Laboratory, Model CTP579-15). In both instances, the entirety of the phantom was scanned using the parameters listed in Table 1. Scans were performed at 120 kVp in helical mode. Five tube current levels were used: 45 mA, 90 mA, 180 mA, 270 mA, and 350 mA corresponding to $CTDI_{vol}$ levels of 2.5, 5.0, 10.0, 14.9, and 19.4 mGy respectively. For each phantom setup (with/without the ring) ten scans were performed at each tube current with equivalent settings. This provided enough data to account for statistical variations in the measurements.

Protocol	Abdomen/Pelvis WO Contrast
Scan Mode	Helical
kVp	120
Field of View (mm)	240
Pitch	0.813
Tube Rotation Time (s)	0.5
ATCM	Off
Focal Spot Size	Small
Voxel Size (mm^3)	0.468 x 0.468 x 5
Detector Configuration	0.5 mm x 80

Table 1: Data acquisition parameters used.

Each set of raw data was reconstructed using the FBP method and AIDR 3D at the Standard level with filter FC19. These algorithms were readily available on our machine. As FIRST is not yet clinically available on our scanner, the raw data was collected and sent to Toshiba America Medical Systems for reconstruction with FIRST Body and FIRST Body Sharp, both at the Standard level. These scans were then returned for data analysis which was performed using a custom code written in MATLAB (Version R2016b, MathWorks Inc.). Descriptions of the calculations of CT numbers, noise, NPS, and MTF_{task} are found in the following sections.

3.2 IMAGE ANALYSIS: CT NUMBER ACCURACY AND NOISE

The center slice of images corresponding to first module of the ACR phantom were used for CT number accuracy and noise standard deviation calculations. Module 1 contains four cylindrical inserts of differing materials (bone, polyethelene, acrylic, and air) surrounded by water equivalent material (Figure 2). The slice was chosen to avoid the BBs within the phantom as these could affect the HUs of the image, especially for the IR reconstructions.

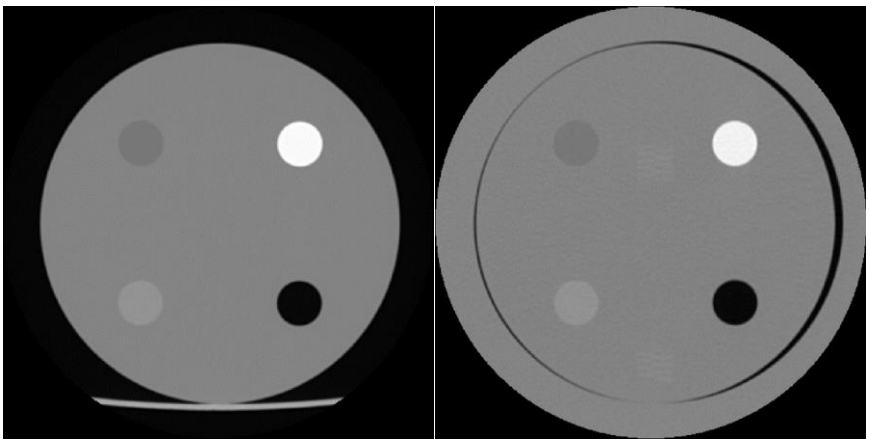

Figure 2: Module 1 of the ACR accreditation phantom without the attenuation ring (left) and with the ring (right).

The center location of each insert was found using The Roberts edge detection method which uses the following equations to compute the sum of the square differences in pixel intensity along the diagonal direction,

$$y_{i,j} = \sqrt{x_{i,j}} \tag{18}$$

$$z_{i,j} = \sqrt{((y_{i,j} - y_{i+1,j})^2 + (y_{i+1,j} - y_{i,j+1})^2} \tag{19}$$

where $x_{i,j}$ is the pixel intensity at location i, j and z_{ij} is the derivative[31]. The result of this process yields a binarized image of the insert edge (Figure 3).

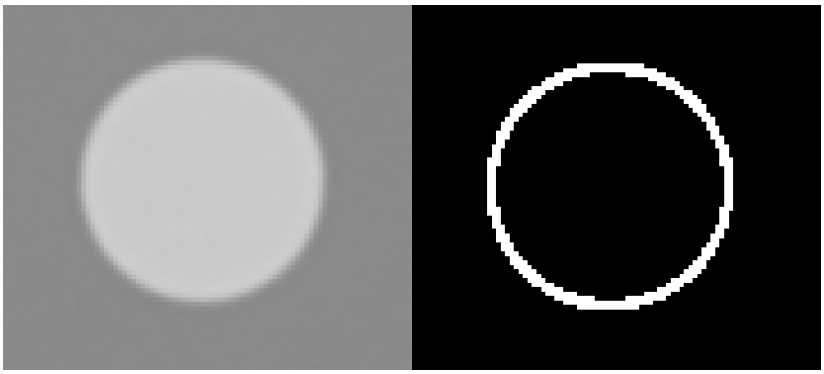

Figure 3: VOI surrounding the bone insert in Module 1 of the ACR phantom (left) and the binarized edge detection image resulting from the Roberts process (right).

From the edge image, the centroid of the insert could be defined. The x and y coordinates were calculated for each insert on images reconstructed with FIRST Body at the highest mA value (350 mA) and without the body ring. This reconstruction algorithm was chosen as it was shown to reduce noise the most in preliminary studies and thus would give the most accurate locations. The calculated locations were then used as the insert centers for all CT accuracy calculations for each reconstruction and dose index combination.

A 30 x 30 pixel (197 mm^2) VOI was placed on the image, centered around each calculated insert center as well as a VOI placed in the water material background at the

same radius from the center of the phantom (Figure 4). The average HU value within each VOI (μ) was recorded along with the standard deviation (σ). The values of μ were averaged over ten scans for each insert and a pooled standard deviation (noise) was calculated from the values of σ by the equation,

$$\sigma^2 = \frac{[(n_1 - 1) * \sigma_1^2] + [(n_2 - 1) * \sigma_2^2] + \cdots + [(n_k - 1) * \sigma_k^2]}{n_1 + n_2 + \cdots + n_k - k} \quad (20)$$

where n_i and σ_i are the number of pixels in and the standard deviation of HUs within the i^{th} VOI respectively[32]. This process was repeated for each reconstruction algorithm and dose level combination.

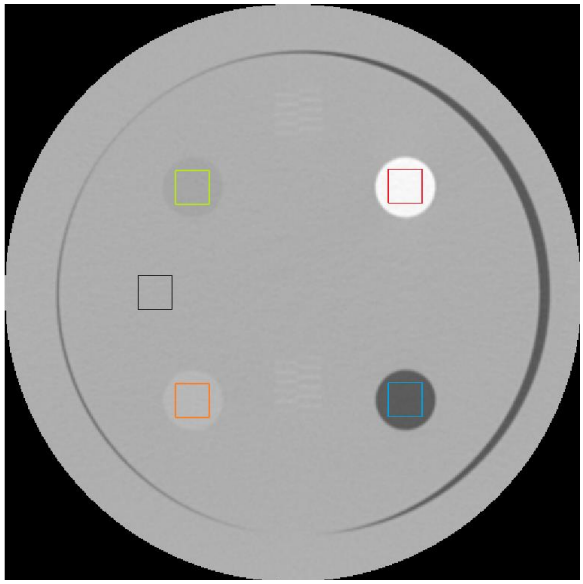

Figure 4: VOI locations in Module 1 of the ACR phantom used for CT number accuracy calculations for each insert: bone (red), polyethylene (green), acrylic (orange), air (blue), and water (black).

3.3 IMAGE ANALYSIS: NOISE POWER SPECTRUM

Ten slices within the third module of the ACR phantom were used for the NPS calculations. This portion of the phantom is used to assess uniformity and provides a large area of solid water to measure noise (Figure 5).

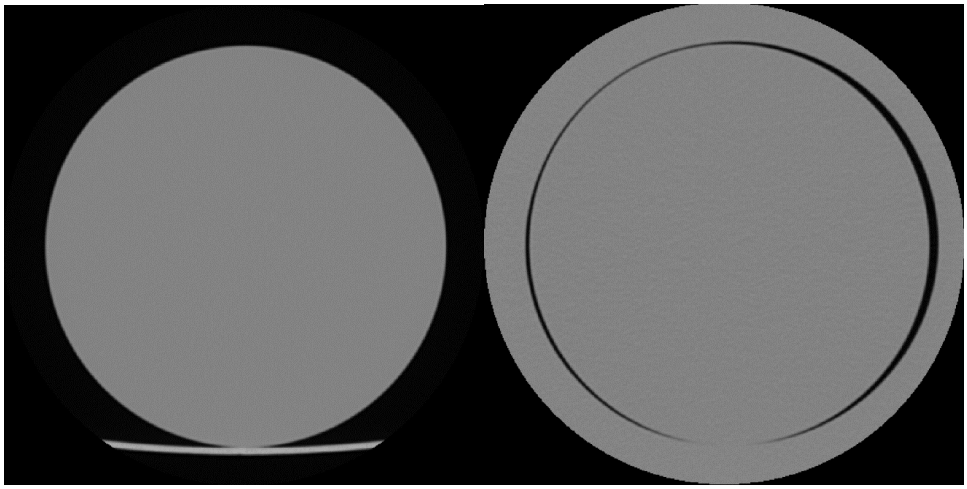

Figure 5: Module 3 of the ACR accreditation phantom used for the NPS analysis, without the body ring (left) and with the body ring (right).

Two consecutive scans, of the same dose level and reconstruction algorithm, were subtracted from one another on a voxel-by-voxel basis, as described by Equation (12), to properly detrend the scan in a 3D manor. This results in five noise only images for each slice position on which the NPS is calculated. A representative noise only image is shown in Figure 6.

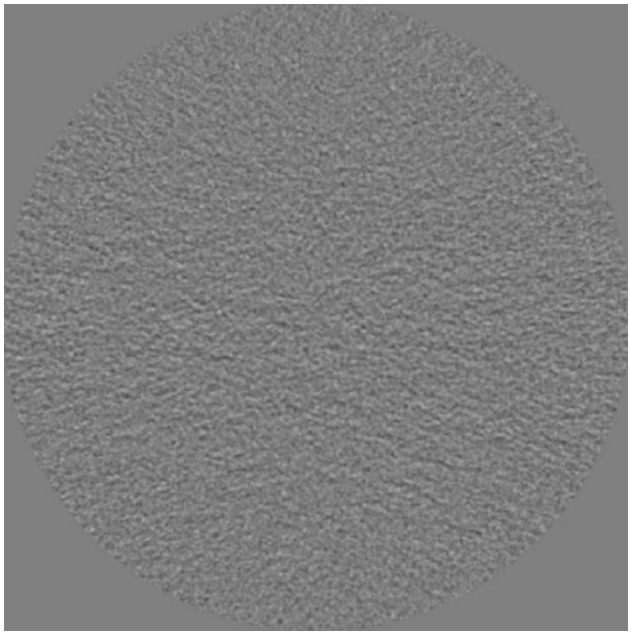

Figure 6: Two consecutive scans at 180 mA reconstructed with AIDR 3D were subtracted to yield this detrended image.

VOIs were placed at a distance equal to half of the phantom radius (5 cm) from the center of the phantom. Each VOI was 128 x 128 x 10 pixels and a total of 32 VOIs were used. Locations of each VOI and a representative VOI are shown in Figure 7. These parameters were used in Equation (13) to calculate the ensemble average of the Fourier transforms calculated over all the VOIs, yielding the 3D NPS. The 2D NPS was extracted from the 3D calculation for when $f_z = 0$. Finally, 1D NPS were calculated by radially averaging the 2D NPS and extracting the NPS in both the x and y directions.

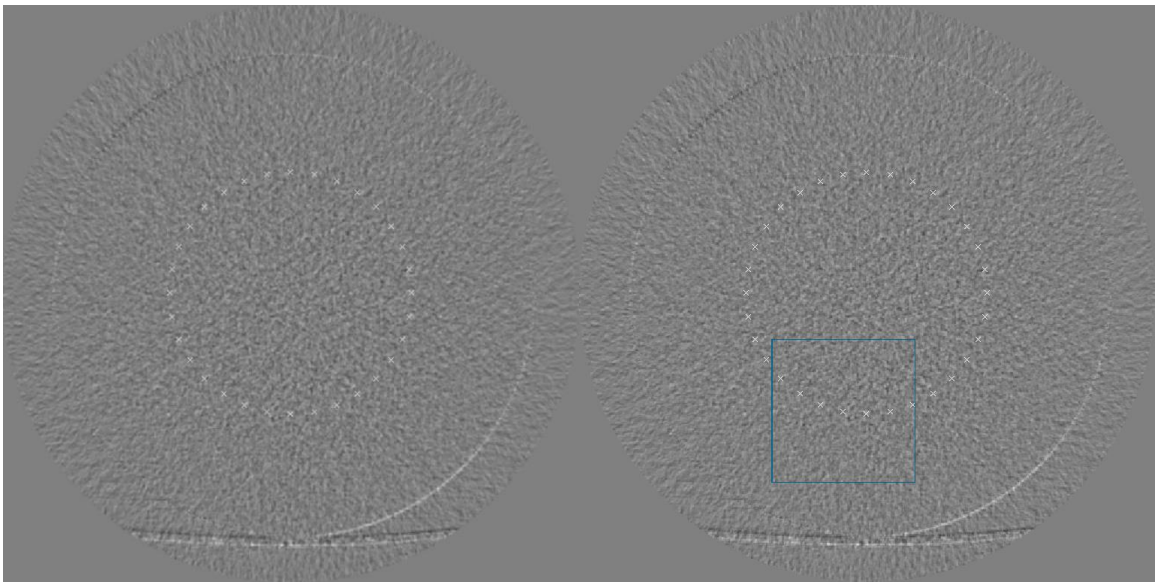

Figure 7: White 'X's mark the locations of the VOIs used in the NPS analysis (left). One VOI boundary shown in blue (right).

3.4 IMAGE ANALYSIS: MODULATION TRANSFER FUNCTION

The MTF_{task} must be calculated on ensemble averaged images to reduce noise aliasing. Six consecutive slices from Module 1 of the ACR phantom were chosen. The images corresponding to a specific slice position were averaged together across all ten scans for a given reconstruction and dose index. This yielded a data set consisting of six low noise images.

The centers of each insert were calculated with the technique explained in section 3.2. An ensemble averaged image with the insert centers marked in shown in Figure 8. With the center of the insert defined, a VOI was drawn around the insert similar to Figure 3.

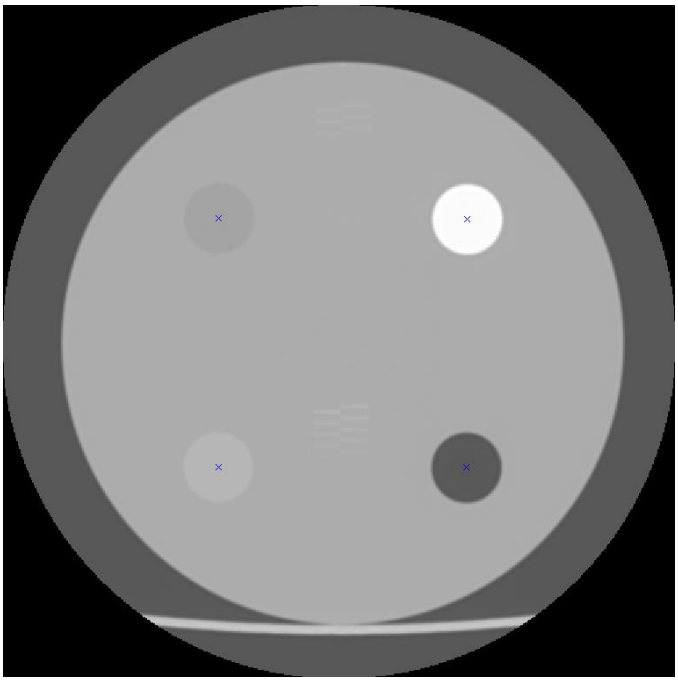

Figure 8: Center pixels of each insert were calculated using edge detection methods. Each insert center is marked with a blue 'X'.

For each pixel within this VOI, the distance to the center of the insert was calculated by,

$$r_{i,j} = \sqrt{(x_{i,j} - x_{\text{center}})^2 + (y_{i,j} - y_{\text{center}})^2} \tag{21}$$

where $x_{i,j}$ and $y_{i,j}$ define the pixel location and x_{center} and y_{center} define the center of the insert. This distance was stored along with the HU of each pixel. When sorted by distance from the insert center, these values yield the ESF of the insert (Figure 9). Binning was performed on the data based on the size of one pixel.

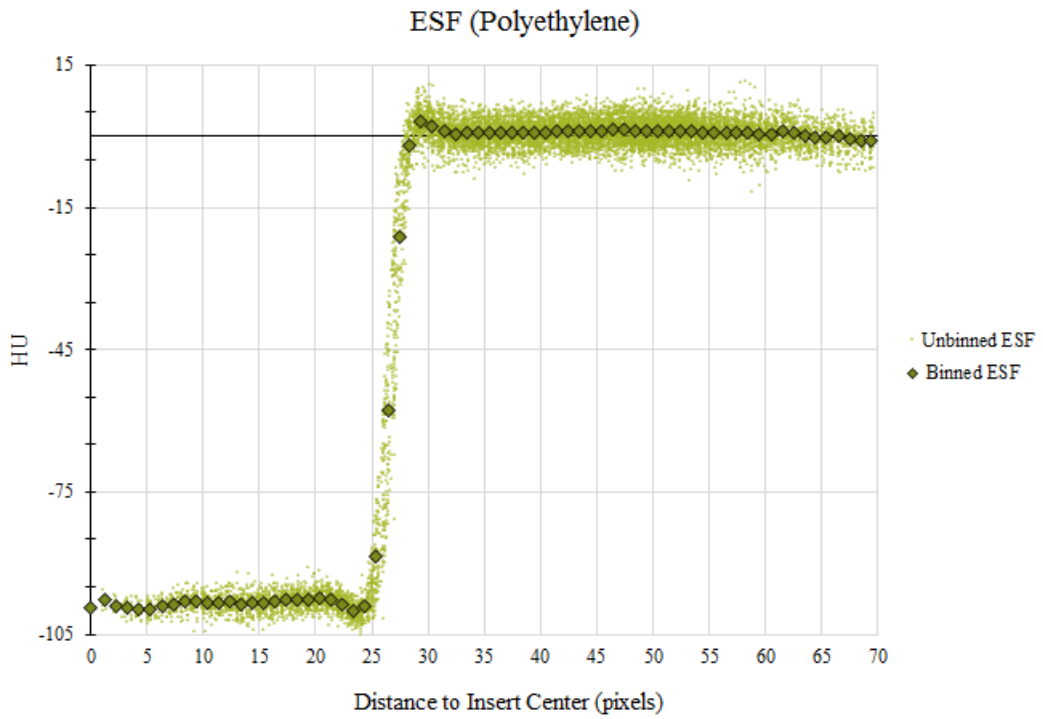

Figure 9: Edge spread function of the polyethylene insert for AIDR 3D at 180 mA.

The ESF was next differentiated to yield the LSF (Equation (16)) and normalized by the area under the LSF curve (Figure 10). The LSF was calculated on each slice of the ensemble average. These values were then averaged to yield the final LSF for the insert. The tails of the LSF contain no information about the edge and add noise to the MTF_{task}. Thus, the LSF was clipped to only include the peak and a small margin near the peak. These values were then zero-padded for MTF_{task} graphing purposes.

The calculation of the MTF_{task} was performed on the LSF as given by Equation (17). It was then normalized to unity at zero frequency. Determination of the frequency corresponding to 10% of the modulation transfer (limiting spatial resolution) was found for each insert. This process was repeated for each contrast material and each reconstruction algorithm and dose index combination.

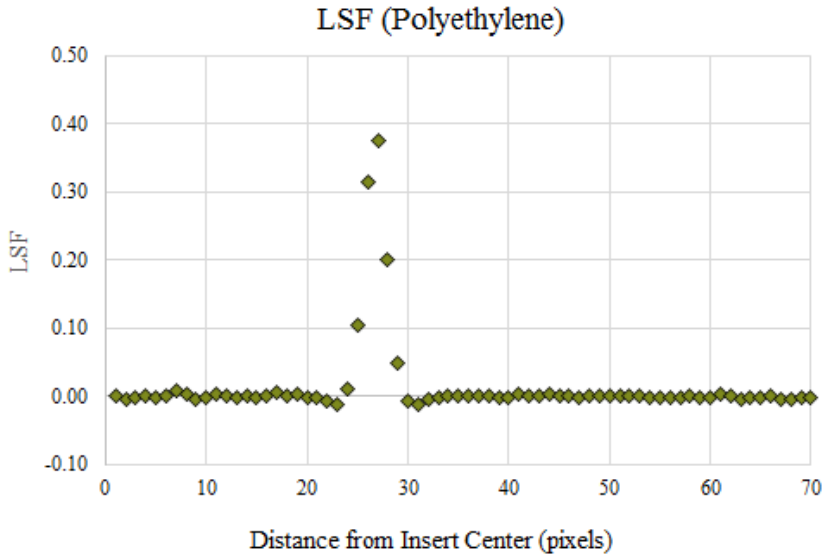

Figure 10: Line spread function of the polyethylene insert for AIDR 3D at 180 mA.

4 RESULTS

4.1 CT NUMBER ACCURACY AND NOISE

The true CT number of each insert is listed in Table 2. In addition, the acceptable accuracy criteria as outlined by the ACR CT accreditation program testing instructions is listed as well as the acceptable deviation from the true CT number. These values are only valid for scans performed without the attenuation ring.

Insert Material	CT Number (HU)	Accuracy Criteria (HU)	Acceptable Deviation from CT Number (HU)
Bone	955	850 – 970	-105 – 15
Acrylic	120	110 – 135	-10 – 15
Water	0	-7 – 7	-7 – 7
Polyethylene	-95	-107 – -84	-12 – 11
Air	-1000	-1005 – -970	-5 – 30

Table 2: CT number and accuracy criteria for each insert material as outlined by the ACR CT accreditation program testing requirements. The acceptable deviation is calculated by subtracting the CT number from the accuracy criteria.

Comparisons of CT number accuracy of the acrylic insert between images with and without the body ring are shown in Figure 11. The known HU of acrylic (120 HU) was subtracted from measured values to yield the error in CT number measurement. Values are shown for each tube current level and each reconstruction algorithm. The CT number accuracy values without the ring are well within the ACR accreditation criteria for acrylic (-20 – 15). Without the ring, FBP and AIDR 3D are more accurate at all dose levels. With the ring, FIRST reconstructions are more accurate at higher tube currents and are more consistent overall, while FBP and AIDR 3D are more accurate at low tube currents.

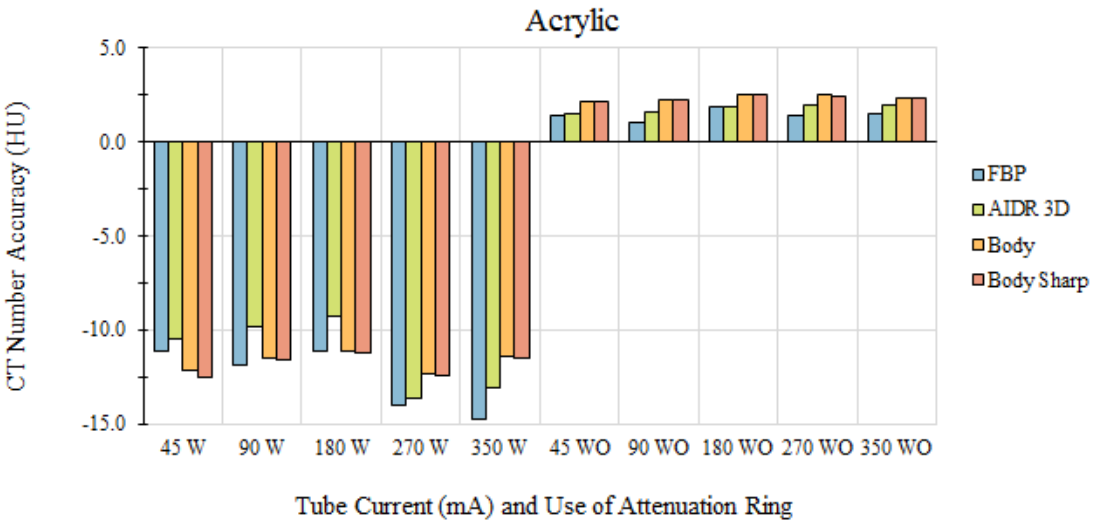

Figure 11: CT number accuracy of each reconstruction algorithm and dose level are shown for images with and without the body ring. FBP and AIDR 3D are more accurate however FIRST reconstructions show consistency.

Without the attenuation ring, all CT number values were well within the ACR accreditation criteria, these measured values can be found in Table 1A in Appendix A. However, because the use of the body ring mimics clinical situations, the CT number values measured when the ring were focused on. Accuracy of each inserts are shown for each reconstruction and dose level in Figure 12. Both FIRST reconstructions show slight improvements in both bone and air CT numbers. For the water, acrylic, and polyethylene

inserts FBP and AIDR 3D are more accurate at the three lowest dose levels. However, FIRST reconstructions again show more consistency with changing tube current.

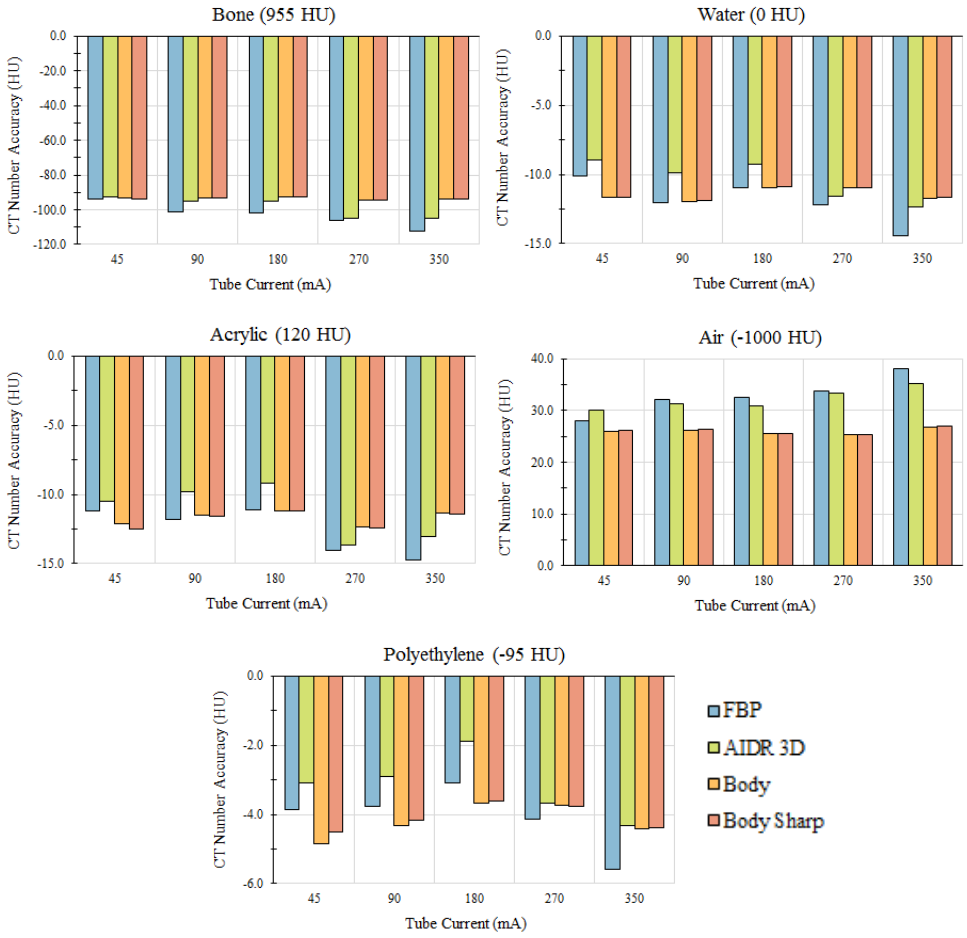

Figure 12: CT number accuracy for each reconstruction and dose index are shown for bone (upper left), water (upper right), acrylic (middle left), air (middle right), and polyethylene (bottom) inserts. Values are shown as the difference between measured and actual CT number. Legend applies to all graphs.

Noise within all inserts was greatly improved with iterative reconstruction techniques as compared to FBP. AIDR 3D reduced noise by values ranging from 25.86-65.29% while FIRST Body reduced noise by 49.27-81.91% and FIRST Body Sharp had a reduction of 28.9-73.76%. As seen in Figure 13, the amount of noise reduction increased

at lower dose levels. FIRST Body had the largest reduction in noise over all inserts and dose levels.

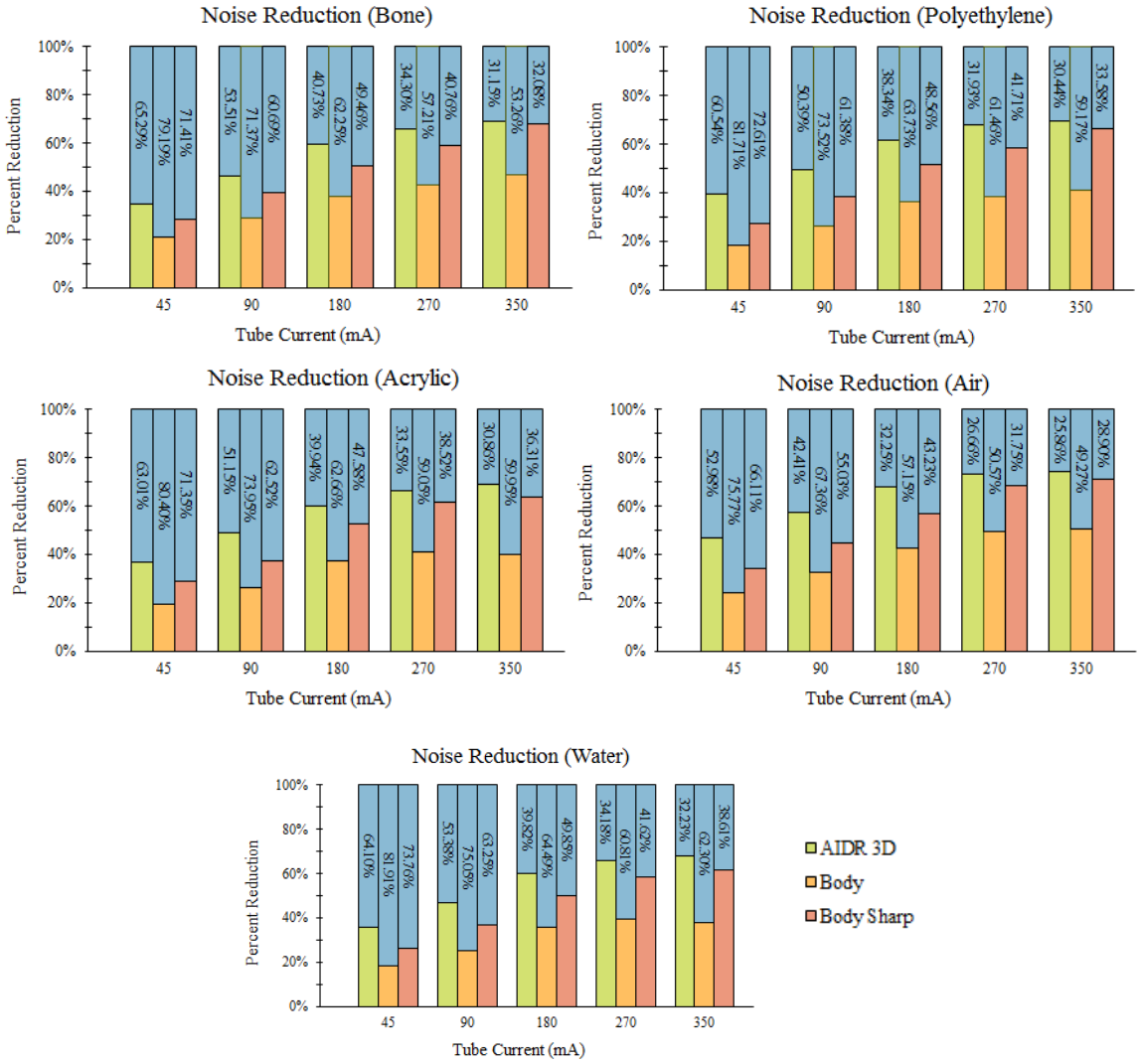

Figure 13: Noise reduction within each insert as a percentage of FBP noise for bone (upper left), polyethylene (upper right), acrylic (middle left), air (middle right), and water (bottom) inserts for each tube current levels. Legend applies to both graphs.

4.2 NOISE POWER SPECTRUM

Figure 14 displays VOIs from detrended images of FBP, AIDR 3D, and FIRST

Body at both 45 and 350 mA. Qualitatively, a large difference in noise texture can be seen between the algorithms. This difference is more pronounced at the lower tube current.

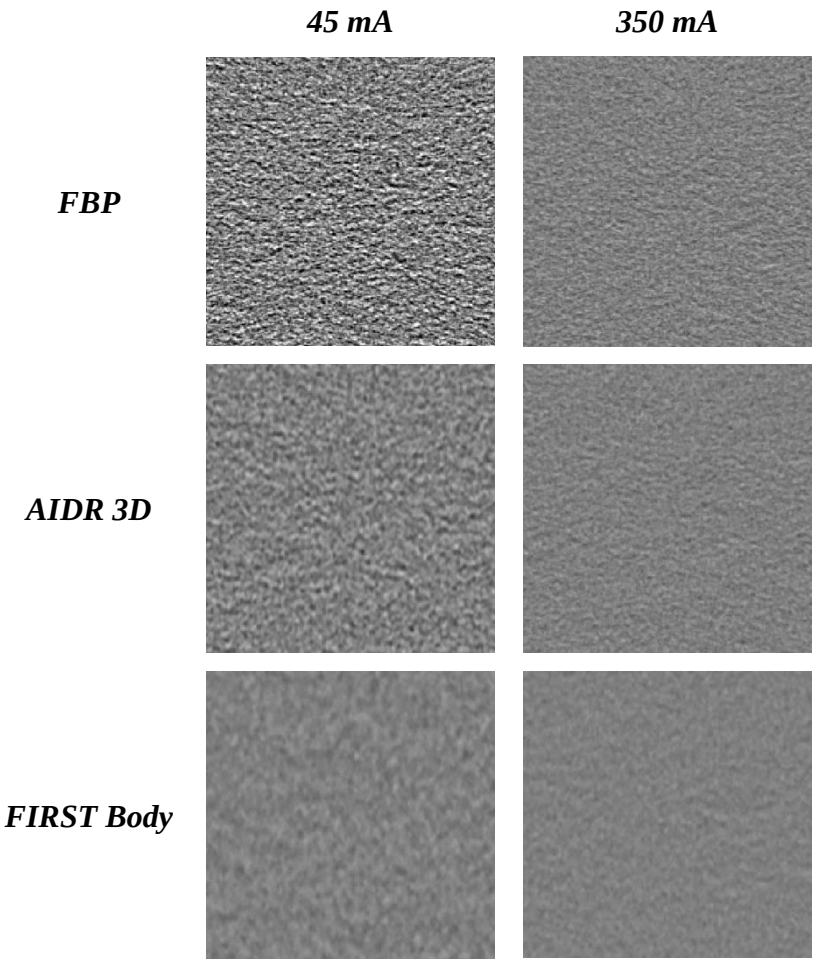

Figure 14: VOIs of detrended images for FBP, AIDR 3D, and FIRST Body at two different tube currents.

Quantitatively, this noise texture can be represented by the noise power spectrum. Figure 15 displays representative cuts of the noise power spectrum at $f_z = 0$ for scans not using the attenuation ring at 180 mA. From visual inspection of these images it is noticed that FBP has the highest magnitude of noise while FIRST Body has the lowest. In addition, FBP has a larger noise magnitude in higher frequencies. All reconstructions

have the traditional torus shape of noise. While it may appear that Body Sharp has a high NPS, the frequencies do not extend past a certain boundary and thus are more predictable than FBP.

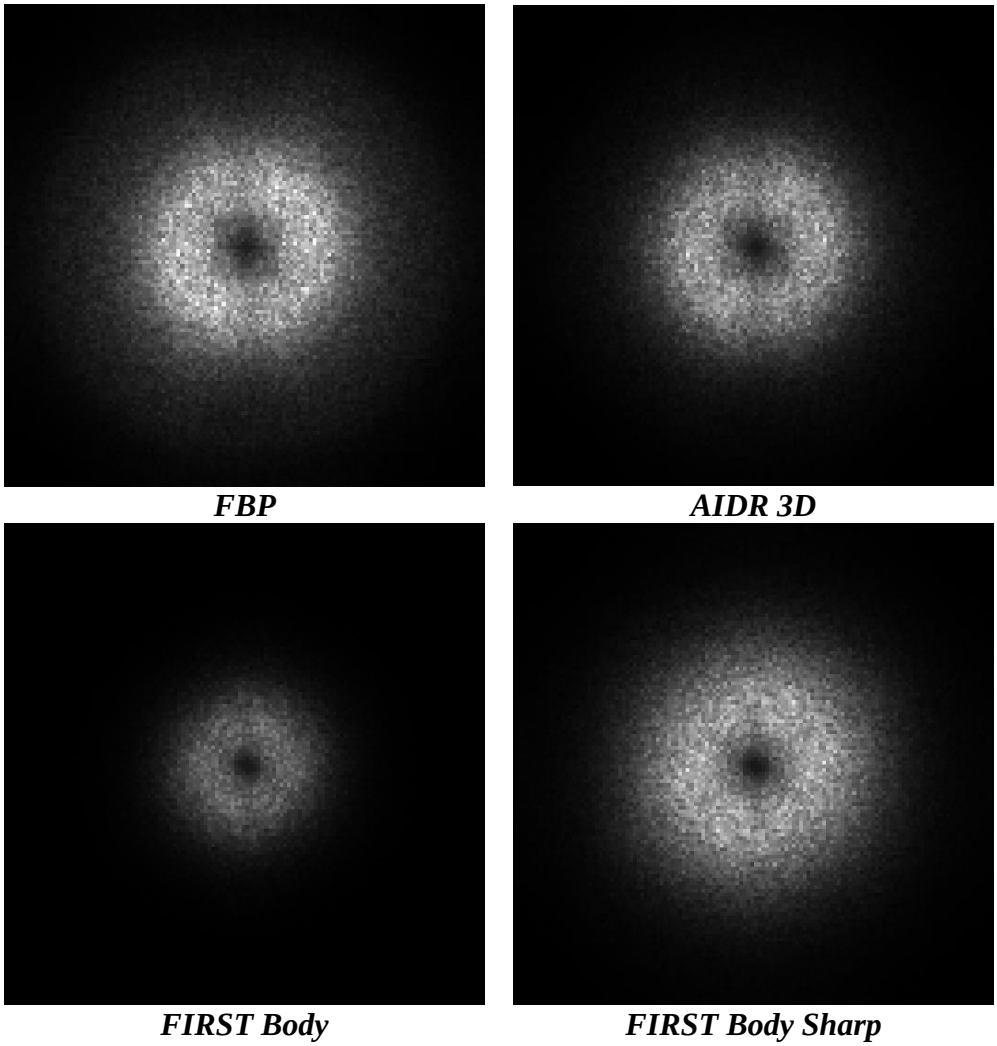

Figure 15: The NPS at $f_z = 0$ for each reconstruction algorithm at 180 mA and no attenuation ring (display range [0 94]).

Phantom scans with the body ring had more attenuating material along one direction. Because of this, the noise magnitude increases in this direction, as seen Figure 16. Similar to Figure 15, the magnitude of noise in the FBP reconstruction is much larger. The NPS of both FIRST Body and FIRST Body Sharp are much more radially

symmetric. It is important to note the images in Figure 15 and Figure 16 are of different display ranges and should not be compared with each other directly.

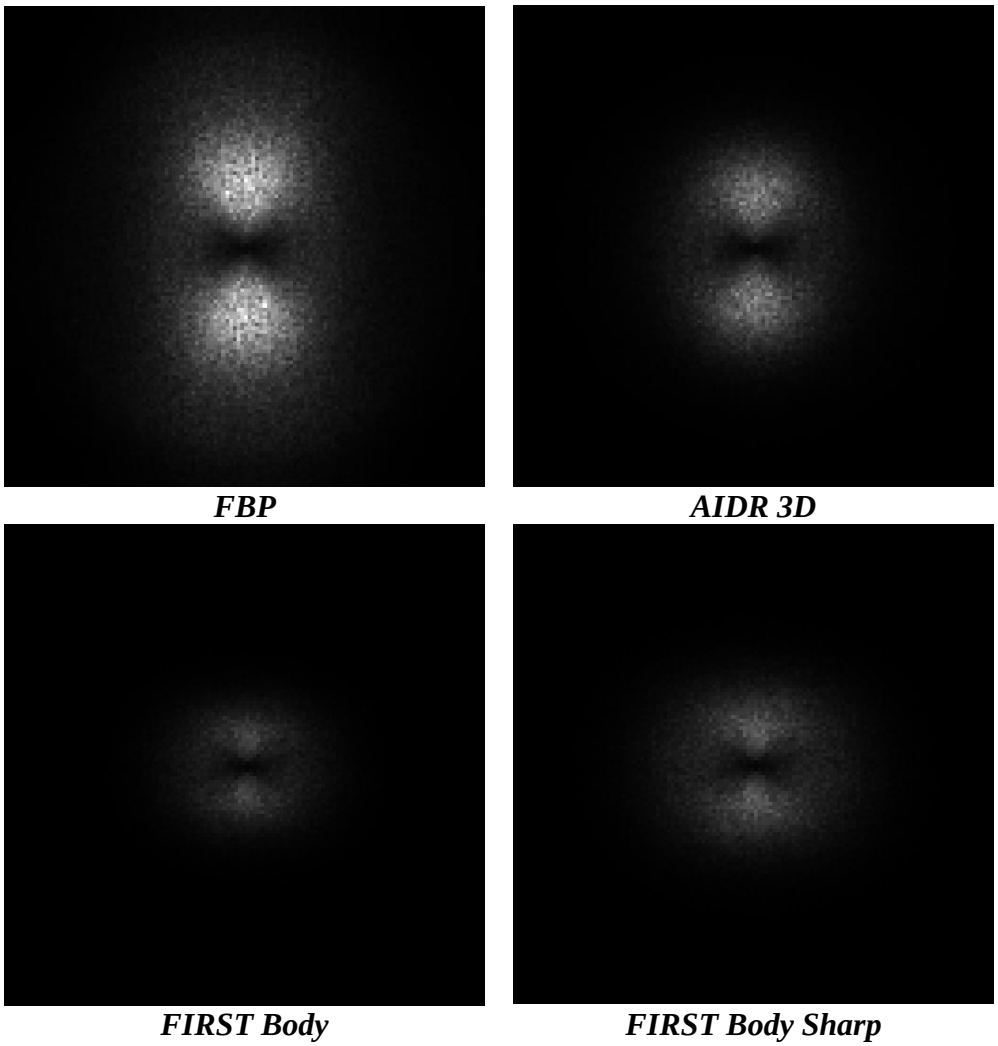

Figure 16: The NPS at $f_z = 0$ for each reconstruction algorithm at 180 mA and with the attenuation ring (display range [0 1341]).

The results of radially averaging the NPS for each algorithm and dose level are shown in Figure 17. Because the large difference in NPS between x and y would affect the radially averaged NPS, all values were calculated on images from scans without the attenuation ring. Plots for each algorithm includes curves for each tube current level. As

expected, the NPS of FBP has a much higher magnitude than any other reconstruction algorithm. AIDR 3D and FIRST Body Sharp have similar characteristics while FIRST Body has the lowest magnitude of noise for all tube currents. An important feature to notice in the radially averaged plots is frequency at which the NPS approaches zero. The NPS values approach zero before $f_r = 0.4$ (mm^{-1}) for FIRST Body at all tube currents while values do not approach zero until $f_r = 0.6$ (mm^{-1}) for FBP, AIDR 3D, and FIRST Body Sharp which in addition have a larger peak magnitude.

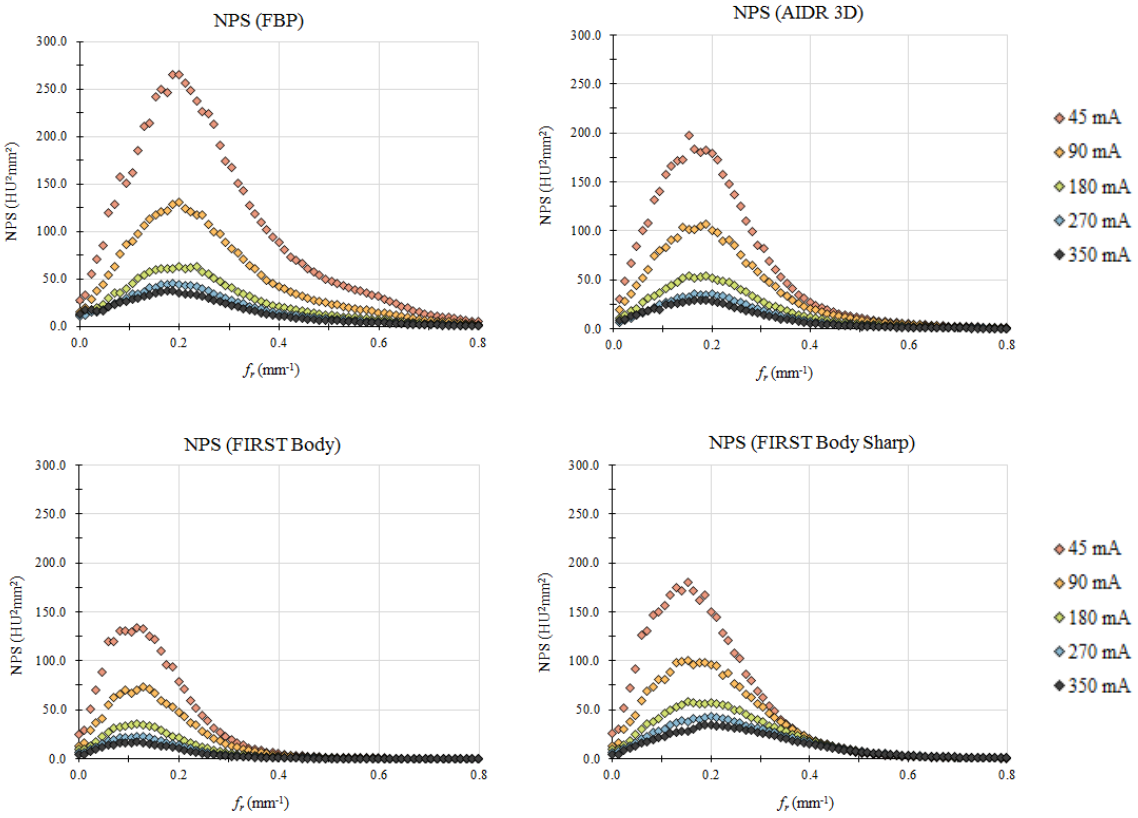

Figure 17: Radially averaged NPS are shown for each reconstruction algorithm and tube current.

A comparison of NPS for differing reconstruction algorithms is shown in Figure 18. At 350 mA, the NPS for FBP, AIDR 3D and FIRST Body Sharp are essentially equivalent. In contrast, FIRST Body shows a large reduction in NPS magnitude as well as

a shift in peak frequency from the other algorithms. With a tube current of 45 mA, this relationship becomes more pronounced. At this tube current, FIRST Body has a magnitude around half the magnitude of FBP and has a peak frequency that is shifted to lower frequencies (and thus larger object sizes).

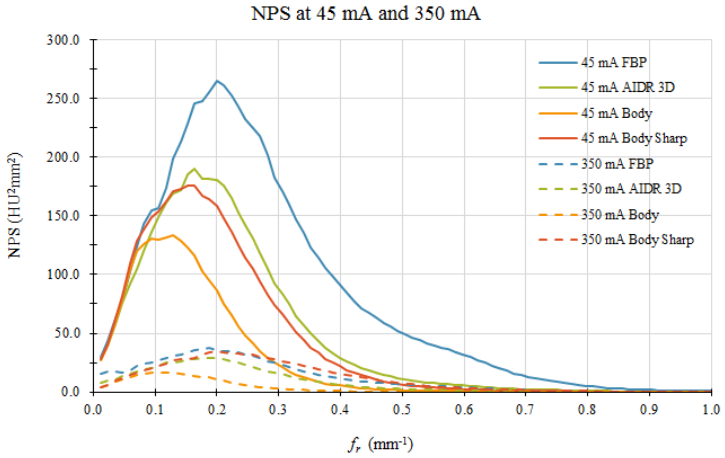

Figure 18: Radially averaged NPS are shown for each reconstruction algorithm for tube currents of 45 mA and 350 mA. Curves are a moving average of the NPS points.

To further investigate the curves shown in Figures 17 and 18, the peak frequency of each NPS was found. The results are shown in Table 3 and Figure 19. FIRST Body had the minimum peak radial noise frequency at all dose levels and was also extremely consistent. At most dose levels, FIRST Body Sharp had a peak frequency similar to AIDR 3D. The peak frequency of FBP varied widely depending on dose index.

Tube Current (mA)	FBP	AIDR 3D	FIRST Body	FIRST Body Sharp
45	0.188	0.153	0.117	0.153
90	0.200	0.188	0.129	0.153
180	0.235	0.188	0.117	0.153
270	0.188	0.164	0.117	0.200
350	0.176	0.188	0.117	0.188

Table 3: Peak frequency values (mm^{-1}) for each reconstruction algorithm at each tube current level.

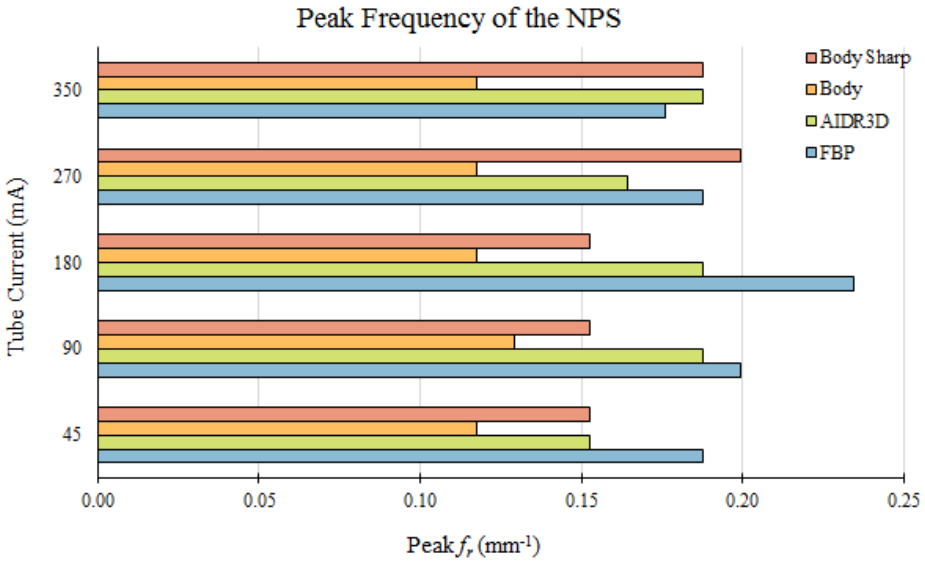

Figure 19: Radial frequencies of the peak noise are displayed for each reconstruction algorithm and dose level.

When the attenuation ring was used on the phantom, the NPS in the x and y directions had much different magnitudes. Comparisons of the xNPS and yNPS are shown in Figure 20. Although there are differences between xNPS and yNPS for all algorithms, the x and y curves of FIRST Body are closer in magnitude. This indicates a more radially symmetric NPS which was also seen in Figure 16.

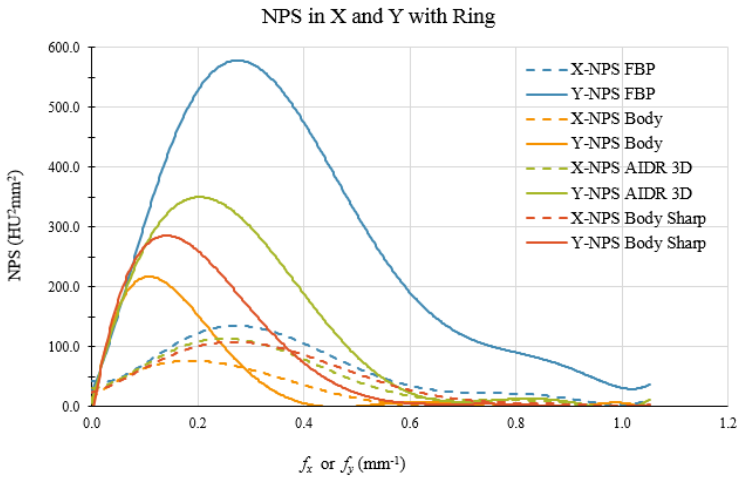

Figure 20: Comparisons of the NPS in the x and y directions is shown for each algorithm at 270 mA. Curves are a polynomial fit.

4.3 MODULATION TRANSFER FUNCTION

Figure 21 shows the MTF_{task} for each algorithm at 180 mA. As expected, the MTF_{task} of IR algorithms have a dependence on contrast whereas the FBP curves are clustered around the same trend for all inserts. The spatial resolution of bone in both FIRST reconstruction algorithms is highly superior. The broad curvature of FIRST algorithms shows a more consistent spatial resolution over many object sizes.

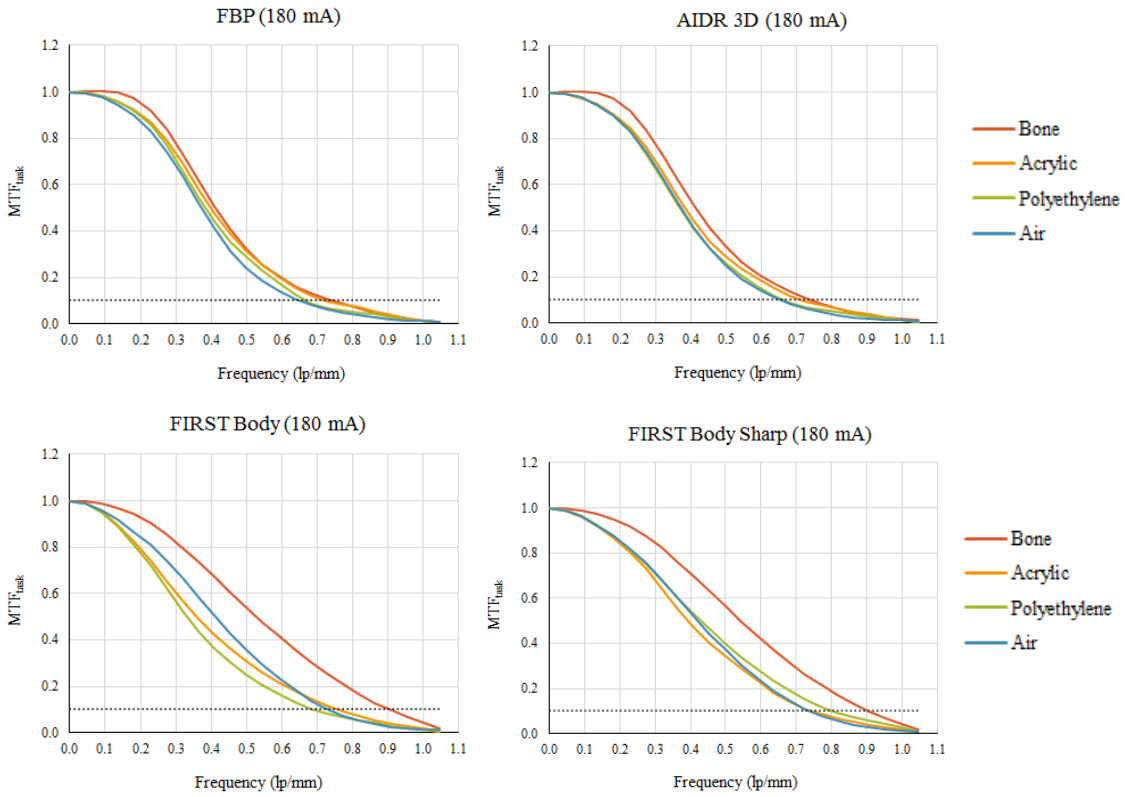

Figure 21: Task-based modulation transfer function curves for each reconstruction algorithm at 180 mA.

A comparison of MTF_{task} values between reconstruction algorithms is shown in Figure 22. There is an obvious improvement in spatial resolution between FIRST and other algorithms for both the bone and air spatial resolution. In the acrylic and polyethylene inserts, the Body Sharp reconstruction algorithm has a slight improvement

in spatial resolution compared to AIDR 3D and FBP. It is evident that the MTF_{task} has a very different shape for all tasks using MBIR.

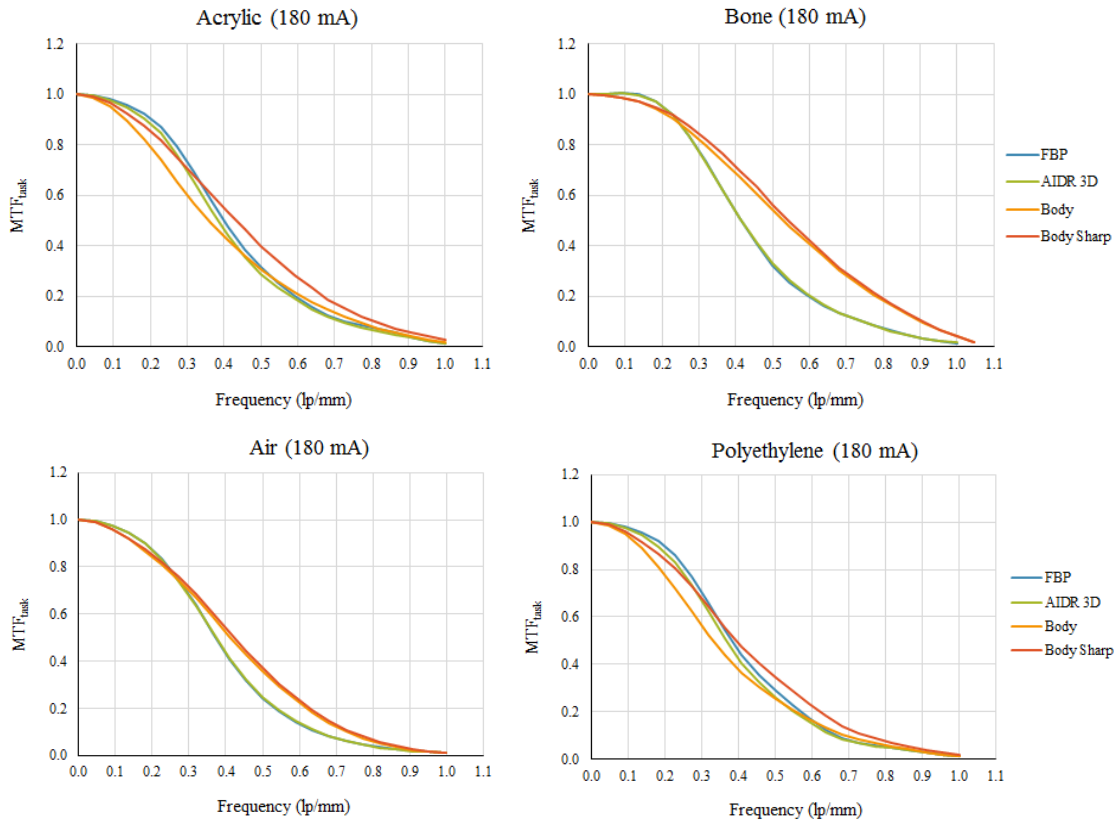

Figure 22: Comparisons of MTF_{task} curves between reconstruction algorithms for the bone (upper left), acrylic (upper right), air (bottom left), and polyethylene (bottom right) inserts at 180 mA. Legend applies to all graphs.

The limiting frequency for each reconstruction algorithm and dose level was found from MTF_{task} plots. The results are displayed in Figure 23. For bone and air inserts, both FIRST algorithms had noticeably larger 10% frequencies for all tube currents. In the polyethylene and acrylic inserts, FBP performed better at the lowest dose index while FIRST performed better at both 180 and 350 mA. Values for every dose level and reconstruction algorithm can be found in Table A2 in Appendix A. The inverse of the

limiting spatial frequency gives the size in the spatial domain (object size) where spatial resolution becomes limited. These results are shown in Figure 24.

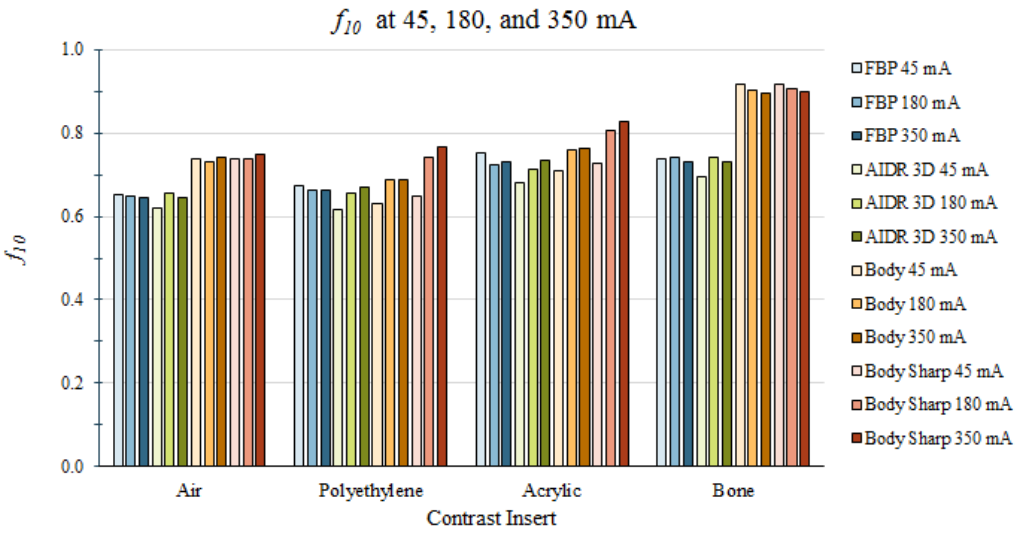

Figure 23: Spatial frequency of 10% of the MTF_{task} curves for each reconstruction algorithm and dose levels of 45, 180, and 350 mA.

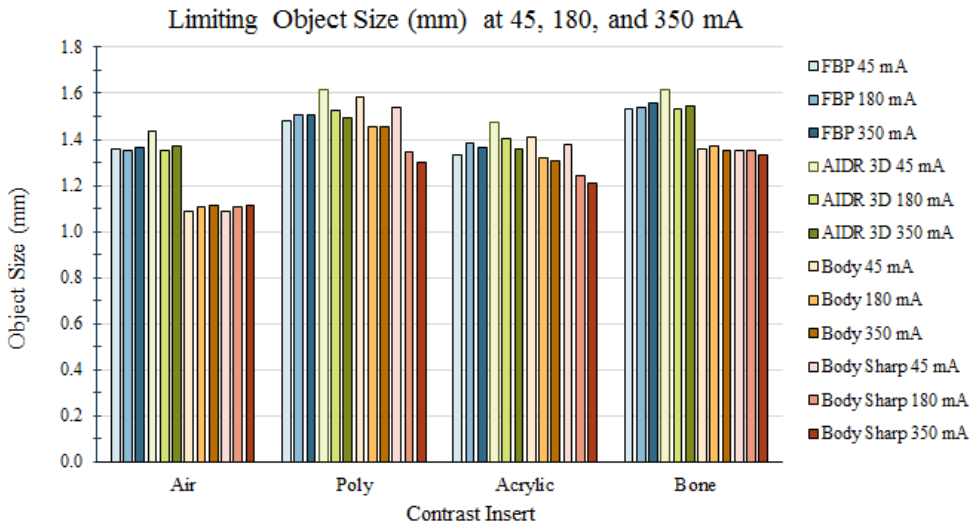

Figure 24: Limiting object size (mm) for each reconstruction algorithm at dose levels of 45, 180, and 350 mA.

In addition to contrast dependence, the spatial resolution of iterative reconstruction techniques also showed a dependence on dose level. Figure 25 shows the MTF_{task} for the polyethylene insert at each tube current level for both FBP and FIRST Body Sharp. The

spatial resolution of FBP is dose independent where the opposite is true for FIRST Body Sharp. The shape and values of MTF_{task} for polyethylene at the lowest tube current (45 mA) for FIRST Body Sharp is similar to the FBP curves.

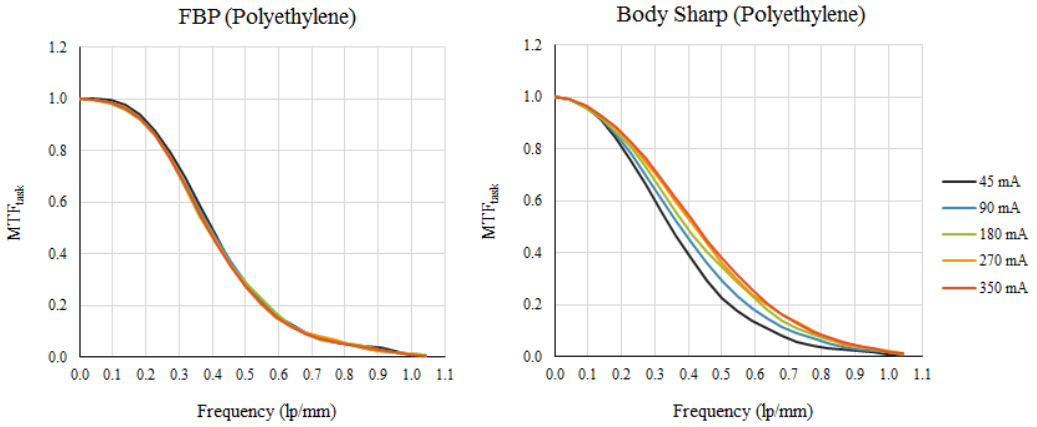

Figure 25: Dose level dependence of FBP and FIRST Body Sharp for the polyethylene insert.

Noise can have a large effect on modulation measurements. This is evident from attempting to calculate the MTF_{task} for scans with the attenuation ring. The ESF and thus the LSF of the acrylic and polyethylene inserts had too much noise to accurately calculate the $MTF_{task.}$ when the body ring was used. Thus, only two MTF_{task} values could be evaluated, bone and air. Figure 26 shows the comparison of spatial resolution for FBP and FIRST Body Sharp when the body ring was used versus when it was not.

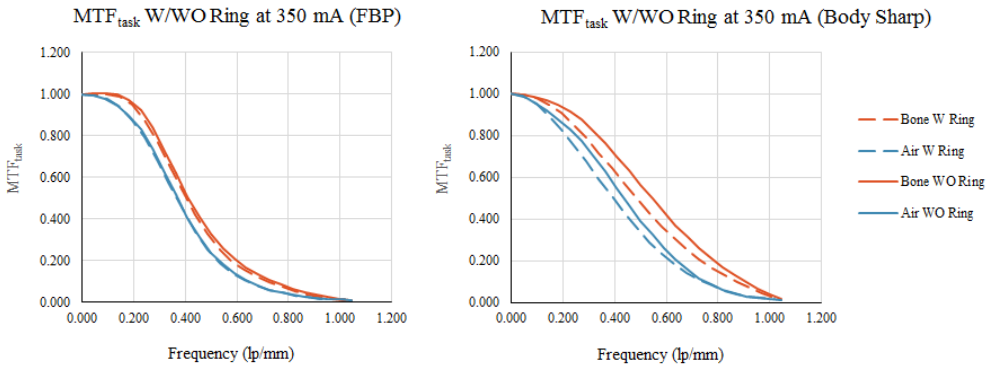

Figure 26: Comparison of MTF_{task} for bone and air inserts with and without the use of the attenuation ring for FBP and Body Sharp.

Although there is a stronger dependence on spatial resolution when using the attenuation ring for the FIRST Body Sharp reconstruction, the limiting spatial frequency with the ring is still larger than for FBP. The comparisons of limiting spatial frequency with the use of the body ring are shown in Figure 27. The limiting frequency of both FIRST reconstructions is higher at all tube currents.

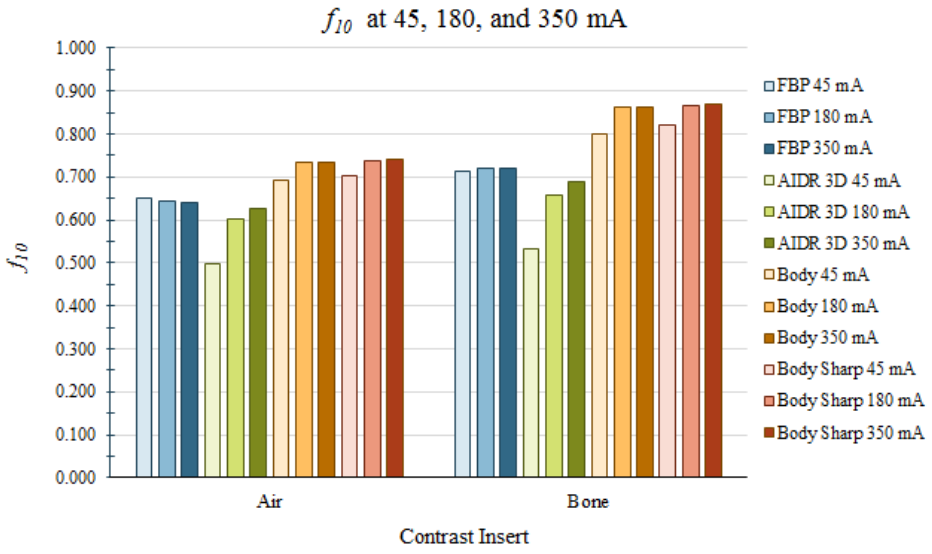

Figure 27: Spatial frequency of 10% of the MTF_{task} for each algorithm and dose levels of 45, 180, and 350 mA when the attenuation ring was used.

5 DISCUSSION

5.1 LIMITATIONS

Before analyzing the results, it is important to note limiting factors of this study. Firstly, while ten scans of the phantom per dose level yields enough data to reduce statistical variations, increasing the number of scans taken per dose level may yield more statistically significant results. Second, a major assumption in CT image quality is that of stationary statistics (shift-invariance). The use of Fourier methods on non-stationary images yields invalid results. While shift-invariance can typically be assumed for FBP,

MBIR algorithms are inherently non-linear. The effects of this can be reduced through utilizing small, localized VOIs and multiple scans as done in this study, however, the results must be analyzed with this fact in mind. And thirdly, the non-linearity of MBIR also effects the reaction of the algorithm to local HU gradients, especially with high contrast materials. Thus, the relatively homogeneous nature of the ACR phantom may not fully predict the outcome of the algorithm in a clinical setting although it provides a starting point for clinical translation.

5.2 CT NUMBER ACCURACY AND NOISE

Although CT number accuracy is used to analyze CT system performance, clinically, the accuracy of HU units helps differentiate between adjacent materials. Thus, the measurements using the attenuation ring provide information on how each reconstruction algorithm performs. The comparisons of acrylic CT number show that use of the attenuation ring can greatly change how a material is perceived (Figure 11). Without the ring, all CT numbers were greater than the true HU, while with the use of the ring all CT numbers were below 120 HU. This of course can be due to increased noise in the image. However, this increased noise will be seen in clinical images and thus analysis using the ring is more informative for protocol optimization.

The CT number of the bone and air inserts was more accurate with FIRST reconstructions over all tube currents (Figure 12). However, for lower contrast materials such as water, polyethylene, and acrylic, FIRST reconstructions were less accurate at presenting the true HU (Figure 12). Nevertheless, the CT number error was more consistent over differing dose levels for FIRST. This is important when considering the

wide range of scanning protocols used to produce images. A more consistent HU can provide a working understanding of material analysis for radiologists that does not vary with dose level.

The large reduction in noise within each insert is evident based on the measurements taken in this study (Figure 13). FIRST Body can reduce noise in polyethylene by over 80% as compared to filtered backprojection. While this is an impressive number, the reduction in noise needs to be coupled with accuracy in CT number as well as spatial resolution in order to be applicable. Because of the consistency of CT number accuracy seen, especially considering the accuracy is close to that seen in FBP, the reduction in noise should improve image quality.

5.3 NOISE POWER SPECTRUM

Like the noise reduction seen within the Module 1 inserts, the noise power spectrum results show the immense noise reduction potential of FIRST Body. This is seen both qualitatively from the NPS images (Figure 14), as well as in the radially averaged plots (Figure 17). With this level of noise reduction, it may be possible to reduce the tube current, and thus the patient dose, while maintaining the same level of noise which in turn maintains or improves spatial resolution.

In this study, we did not use automatic tube current modulation (ATCM). The NPS using the attenuation ring may differ if ATCM was used due to the increased number of photons in the more attenuating direction. However, the NPS results with the ring show that FIRST has mechanisms which distribute noise more uniformly across the image even without the use of ATCM. This is evidenced by the increased radially

symmetry seen in Figure 16*: The NPS at $f_z = 0$ for each reconstruction algorithm at 180 mA and with the attenuation ring (display range [0 1341]).* and Figure 20*: Comparisons of the NPS in the x and y directions is shown for each algorithm at 270 mA. Curves are a polynomial fit.*.

As seen in Figure 17, the magnitude of the NPS curve for 45 mA of FIRST Body is similar to the peak of 90 mA for FBP. The equivalency of these values yields a way to optimize and implement FIRST Body protocols in clinical use. For example, protocols using a tube current of 45 mA and FBP as the current clinical standard could have dose reduction of ~50% with a similar or even reduced noise profile with FIRST Body. Another important finding from Figure 17 is the tail of each curve and at which frequency it approaches zero. For example, the tail of FIRST Body at 90 mA drops quickly to zero whereas the tail of 90 mA for FBP stretches into larger frequency values. This indicates there will be more noise at smaller object sizes which may make diagnosis of small lesions or seeing small details more difficult.

The dose reduction potential, in terms of maintaining noise properties, is again apparent from the results shown in Figure 18. At higher tube currents the noise magnitude between algorithms is similar especially for FBP, AIDR 3D, and FIRST Body Sharp. However, as the tube current is decreased, a distinct difference between algorithms appears. This could give justification for the implementation of FIRST Body for clinical situations needing noise reduction, especially for those in which noise at lower tube currents tends to be the limiting clinical factor. An important example of this is pediatric studies in which CT dose is greatly reduced and radiologists are accustomed to noisy images.

This is important in clinical applications as the frequency at which peak noise occurs correlates to the size of objects which will be the noisiest. The results of the peak frequency analysis (Figure 19) show the peak noise occurs at much lower frequencies for FIRST Body. As lower frequencies correlate to larger objects, smaller objects will be less noisy as compared with FBP, possibly lending to increased small lesion detection and other applications which require analysis of small detail. In addition, FIRST Body had the most consistent peak noise frequency over all tube potentials. Radiologists could thus become accustomed to a more uniform noise texture for multiple imaging protocols.

5.4 MODULATION TRANSFER FUNCTION

The displayed contrast dependence of IR spatial resolution (Figure 21) can propose an intricate problem for clinical applications due to the inherent complexity of anatomy. However, in this study it was shown that at all dose indices the limiting spatial resolution of FIRST Body Sharp was superior to both FBP and AIDR 3D (Figure 23). This was true for all categories except low dose polyethylene and acrylic which mimic materials in the body such as liver tissue. For these contrasts levels, although FIRST reconstructions were not superior, they were similar in magnitude to FBP and AIDR 3D at these doses and were superior at middle and high doses. The spatial resolution of bone and air easily surpass FBP and AIDR 3D indicating that spatial resolution in clinical applications in the thorax may be greatly improved with FIRST. However, the contrast dependency of MBIR will change the method in which detail is viewed in CT images.

The limiting spatial frequency (f_{10}) is commonly used at the metric to compare spatial resolution. The measured values are shown in Figure 23 as well as a full list in

Table A2 in Appendix A. For a low dose, low contrast situation (45 mA and acrylic), the limiting spatial frequency of AIDR 3D was 0.680 mm^{-1} while for FIRST Body Sharp it was 0.727 mm^{-1}. These values correspond to object sizes of 1.471 mm and 1.376 mm respectively showing that FIRST Body Sharp can resolve smaller objects in the image. This result is also seen in Figure 24 in which the limiting object size for each material are shown. FIRST Body Sharp is superior in every category except low dose (45 mA) polyethylene and acrylic for which FBP was able resolve smaller objects.

Adding to the complexity of the contrast dependent spatial resolution, FIRST also exhibited a dose level dependence as seen in Figure 25. However, the lowest dose level MTF_{task} for polyethylene was similar in shape and magnitude to FBP, showing FIRST will have equivalent or improved spatial resolution. Similarly, the findings utilizing the attenuation ring demonstrate that the spatial resolution of FIRST has a larger dependence on patient size (Figure 26). Still, the minimal MTF_{task} values for FIRST Body Sharp were either equivalent or superior to that of FBP without the ring. As bone and air were the only inserts in which this comparison could be performed, further analysis of this finding is necessary for it to be conclusive.

An important characteristic shown by spatial resolution analyses is the shape of the MTF_{task} curves. Rather than having a rounded peak at low frequencies that drops quickly, the MTF_{task} for FIRST reconstructions is more linear with frequency. This indicates spatial resolution will be more uniform across multiple object sizes.

6 CONCLUSIONS

6.1 FUTURE DIRECTIONS

The following paragraphs describe possible future studies aimed at further understanding the image characteristics of FIRST. Many of these could be performed using the ACR CT accreditation phantom. However, increasing the phantom complexity (i.e. anthropomorphic phantoms) or using human subjects or cadavers would drive the MBIR algorithm into more clinically relevant modes.

The analysis of stationary statistics within localized regions of FIRST Body and FIRST Body Sharp would give validation to many of the assumptions given in this work. This could be performed using Module 3 of the ACR phantom and assessing VOIs with differing sizes and radii from the center of the phantom.

Due to the inherent non-linearity of MBIR, measurements using a phantom are only valid with specific conditions and assumptions. To combat this, an observer study would provide information on the clinical utility of the algorithms as evaluated by professional readers (such as radiologists or medical physicists). Analysis could be performed using real clinical images, scans of cadavers, or with images of an anthropomorphic phantom each reconstructed with both FBP, AIDR 3D, and FIRST. If these results can also be matched with quantitative analysis such as those performed in this work, the connections between Fourier image quality assessment and desired clinical image quality can be formulated for MBIR.

Repeating these measurements on images with a smaller slice thickness could yield

more information. This research utilized images with a slice width of 5 mm as this used clinically. However, because of this, the 3D NPS for $f_x = 0$ and $f_y = 0$ do not contain enough information to fully analyze. If images with slice widths of 1 mm were utilized this could yield more z-axis noise information.

A comparison of FIRST algorithms with other MBIR is important. It could not be completed in this work as other quantitative analyses of MBIR utilized different metrics or only provided graphical figures rather than numerical values such as the limiting spatial resolution. However, the novel power law, $\sigma^2 \propto \text{mas}^{-\beta}$ found by Li et al. and validated by Gomez-Cardona et al., defines a difference between FBP and IR algorithms[24,27]. The determinations of βvalues for FIRST may give one way to compare MBIR algorithms in terms of noise reduction potential.

A daunting task for the implementation of MBIR techniques is protocol optimization. Because of its linear nature, protocol optimization for FBP was relatively straight-forward. However, due to the many factors that affect image quality of MBIR, this task becomes much more complicated. A technique for deciding which factors are important for differing clinical tasks and a new workflow for protocol decision making for MBIR would aid the implementation of MBIR in practice.

6.2 CONCLUSION

The experimental findings in this study provide a quantitative starting point for exploring clinical implementation of FIRST reconstruction algorithms. Overall, this research found FIRST to yield images with more consistent image quality over many dose levels and material makeup as compared with FBP and AIDR 3D. As noise and

spatial resolution are inherently related, and potentially even more so with MBIR, further measurements such as those performed here are necessary to fully understand the clinical potential of these algorithms and to provide robust reasoning for their application. In addition, although the merit of quantitative analysis given through physics research is undeniable, the implementation of MBIR will eventually fall onto the responsibility of radiologists, radiology technicians, and radiology departments to champion clinical implementation and undertake protocol optimization.

With the combination of the FIRST Body and FIRST Body Sharp, the protocols of seemingly all clinical applications could become optimized as evidenced by this research. The noise standard deviation reduction potential of FIRST Body was shown for all material inserts, reducing the noise up to 80% from FBP at low doses. This potential is also seen in the NPS curves in which the FIRST Body curve for 45 mA was similar to that of FBP at 90 mA, indicating a dose reduction potential of ~50%. In addition, the spread of FIRST Body does not extend into high frequencies and had a smaller magnitude than all other algorithms at every dose level. While FIRST Body could greatly improve noise properties, FIRST Body Sharp maintains the noise properties seen with AIDR 3D while greatly improving spatial resolution, both with linearity and limiting object size. Depending on clinical application, either noise or spatial resolution properties can be preferred through the selection of either FIRST Body or FIRST Body Sharp.

The CT number accuracy, noise properties, and spatial resolution of the four reconstruction algorithms varied greatly based on dose level and the use of the attenuation ring. The noise reduction potential of FIRST Body lends itself to improving clinical applications in which noise is an issue. Similarly, the spatial resolution of FIRST

Body Sharp was superior over a wide range of possible contrast and dose levels. to improve patient care in radiology and reduce radiation dose to the population.

REFERENCES

1. Bushberg, J. T., Seibert, J. A., Leidholdt, E. M. & Boone, J. M. *The Essential Physics of Medical Imaging*. (Lippincott Williams & Wilkins, 2011).
2. *Ionizing radiation exposure of the population of the United States: recommendations of the National Council on Radiation Protection and Measurements*. (National Council on Radiation Protection and Measurements, 2009).
3. 2016 CT Market Outlook Report. *IMVInfo.com* Available at: http://www.imvinfo.com/index.aspx?sec=ct&sub=dis&pag=def&itemid=200081. (Accessed: 29th March 2017)
4. Brenner, D. J. *et al.* Cancer risks attributable to low doses of ionizing radiation: Assessing what we really know. *Proc. Natl. Acad. Sci.* **100,** 13761–13766 (2003).
5. Hall, E. J. & Brenner, D. J. Cancer risks from diagnostic radiology. *Br. J. Radiol.* **81,** 362–378 (2008).
6. Sharma, D., Newman, T. G. & Aronow, W. S. Lung cancer screening: history, current perspectives, and future directions. *Arch. Med. Sci. AMS* **11,** 1033–1043 (2015).
7. Liu, L. Model-based Iterative Reconstruction: A Promising Algorithm for Today's Computed Tomography Imaging. *J. Med. Imaging Radiat. Sci.* **45,** 131–136 (2014).
8. Geyer, L. L. *et al.* State of the Art: Iterative CT Reconstruction Techniques. *Radiology* **276,** 339–57 (2015).
9. Padole, A., Ali Khawaja, R. D., Kalra, M. K. & Singh, S. CT radiation dose and iterative reconstruction techniques. *AJR Am. J. Roentgenol.* **204,** W384-92 (2015).

10. Kim, H. J., Yoo, S.-Y., Jeon, T. Y. & Kim, J. H. Model-based iterative reconstruction in ultra-low-dose pediatric chest CT: comparison with adaptive statistical iterative reconstruction. *Clin. Imaging* **40,** 1018–1022 (2016).
11. Shuman, W. P. *et al.* Standard and reduced radiation dose liver CT images: adaptive statistical iterative reconstruction versus model-based iterative reconstruction-comparison of findings and image quality. *Radiology* **273,** 793–800 (2014).
12. Nakamoto, A. *et al.* Clinical evaluation of image quality and radiation dose reduction in upper abdominal computed tomography using model-based iterative reconstruction; comparison with filtered back projection and adaptive statistical iterative reconstruction. *Eur. J. Radiol.* **84,** 1715–1723 (2015).
13. Mueck, F. G. *et al.* How Low Can We Go in Contrast-Enhanced CT Imaging of the Chest?: A Dose-Finding Cadaver Study Using the Model-based Iterative Image Reconstruction Approach: A Dose-Finding Cadaver Study Using the Model-based Iterative Image Reconstruction Approach. *Acad. Radiol.* **22,** 345–356 (2015).
14. Mehta, D., Thompson, R., Morton, T., Dhanantwari, A. & Shefer, E. Iterative Model Reconstruction: Simultaneously Lowered Computed Tomography Radiation Doe and Improved Image Quality. *Med. Phys. Int. J.* **1,** 147–154 (2013).
15. Angel, E. AIDR 3D Iterative Reconstruction: Integrated, Automated, and Adaptive Dose Reduction. (2012).
16. Beister, M., Kolditz, D. & Kalender, W. A. Iterative reconstruction methods in X-ray CT. *Phys. Medica PM Int. J. Devoted Appl. Phys. Med. Biol. Off. J. Ital. Assoc. Biomed. Phys. AIFB* **28,** 94–108 (2012).

17. Braenne, K. R. *et al.* A Liver Phantom Study: CT Radiation Dose Reduction and Different Image Reconstruction Algorithms Affect Diagnostic Quality. [Miscellaneous Article]. *J. Comput. Assist. Tomogr.* **40,** 735–739 (2016).
18. Nishiyama, Y. *et al.* Effect of the forward-projected model-based iterative reconstruction solution algorithm on image quality and radiation dose in pediatric cardiac computed tomography. *Pediatr. Radiol.* **46,** 1663–1670 (2016).
19. Volders, D., Bols, A., Haspeslagh, M. & Coenegrachts, K. Model-based iterative reconstruction and adaptive statistical iterative reconstruction techniques in abdominal CT: comparison of image quality in the detection of colorectal liver metastases. *Radiology* **269,** 469–74 (2013).
20. Joemai, R. M. S. & Geleijns, J. Forward projected model-based Iterative Reconstruction SoluTion 'FIRST'. (2017).
21. ICRU. Report 87. *J. ICRU* **12,** NP–NP (2012).
22. Friedman, S. N., Fung, G. S. K., Siewerdsen, J. H. & Tsui, B. M. W. A simple approach to measure computed tomography (CT) modulation transfer function (MTF) and noise-power spectrum (NPS) using the American College of Radiology (ACR) accreditation phantom. *Med. Phys.* **40,** 051907 (2013).
23. Li, K., Garrett, J., Ge, Y. & Chen, G.-H. Statistical model based iterative reconstruction (MBIR) in clinical CT systems. Part II. Experimental assessment of spatial resolution performance. *Med. Phys.* **41,** 071911 (2014).
24. Li, K. & Tang, J. Statistical model based iterative reconstruction (MBIR) in clinical CT systems: Experimental assessment of noise performance. *Med. Phys.* **41,** (2014).

25. Wilson, J. M., Christianson, O. I., Richard, S. & Samei, E. A methodology for image quality evaluation of advanced CT systems. *Med. Phys.* **40,** 031908 (2013).
26. Dolly, S., Chen, H.-C., Anastasio, M., Mutic, S. & Li, H. Practical considerations for noise power spectra estimation for clinical CT scanners. *J. Appl. Clin. Med. Phys.* **17,** 392–407 (2016).
27. Gomez-Cardona, D. *et al.* Can conclusions drawn from phantom-based image noise assessments be generalized to in vivo studies for the nonlinear model-based iterative reconstruction method? *Med. Phys.* **43,** 687–695 (2016).
28. Richard, S., Husarik, D. B., Yadava, G., Murphy, S. N. & Samei, E. Towards task-based assessment of CT performance: system and object MTF across different reconstruction algorithms. *Med. Phys.* **39,** 4115–22 (2012).
29. Verdun, F. R. *et al.* Image quality in CT: From physical measurements to model observers. *Phys. Med.* **31,** 823–843 (2015).
30. Kofler, J. M. *et al.* Assessment of Low-Contrast Resolution for the American College of Radiology Computed Tomographic Accreditation Program: What Is the Impact of Iterative Reconstruction? *J. Comput. Assist. Tomogr.* **39,** 619–623 (2015).
31. Roberts, L. G. Machine perception of three-dimensional solids. (Massachusetts Institute of Technology, 1963).
32. Rosner, B. *Fundamentals of Biostatistics*. (Cengage Learning, 2010).

APPENDIX A

Bone (-105 – 15)	FBP	AIDR 3D	FIRST Body	FIRST Body Sharp
45 mA	-16.913	-15.813	-10.122	-10.087
90 mA	-17.492	-15.897	-9.259	-9.292
180 mA	-16.185	-15.547	-8.358	-8.380
270 mA	-17.823	-15.169	-8.668	-8.669
350 mA	-17.487	-15.330	-9.438	-9.419

Polyethylene (-12 – 11)	FBP	AIDR 3D	FIRST Body	FIRST Body Sharp
45 mA	-2.875	-2.583	-3.102	-3.086
90 mA	-2.837	-2.540	-2.802	-2.748
180 mA	-2.570	-2.432	-2.742	-2.694
270 mA	-2.907	-2.569	-2.939	-2.892
350 mA	-2.783	-2.500	-3.013	-2.978

Acrylic (-10 – 15)	FBP	AIDR 3D	FIRST Body	FIRST Body Sharp
45 mA	1.436	1.537	2.188	2.159
90 mA	1.007	1.560	2.268	2.261
180 mA	1.910	1.858	2.567	2.524
270 mA	1.398	2.011	2.516	2.485
350 mA	1.476	1.936	2.388	2.303

Air (-5 – 30)	FBP	AIDR 3D	FIRST Body	FIRST Body Sharp
45 mA	16.888	16.863	11.019	11.043
90 mA	16.666	16.343	10.305	10.302
180 mA	16.936	16.569	10.226	10.246
270 mA	17.356	16.286	10.139	10.135
350 mA	17.052	16.325	10.461	10.513

Water (-7 – 7)	FBP	AIDR 3D	FIRST Body	FIRST Body Sharp
45 mA	-0.228	0.053	0.023	0.045
90 mA	-0.229	0.180	0.295	0.299
180 mA	0.214	0.356	0.450	0.460
270 mA	0.050	0.555	0.476	0.501
350 mA	0.089	0.608	0.382	0.412

Table A1: CT number accuracy for scans without the use of the attenuation ring. The acceptable ACR accreditation criteria are also shown for each insert.

Air	45 mA	90 mA	180 mA	270 mA	350 mA
FBP	0.652	0.651	0.649	0.644	0.643
AIDR 3D	0.619	0.651	0.654	0.648	0.646
FIRST Body	0.737	0.734	0.731	0.736	0.741
FIRST Body Sharp	0.739	0.739	0.739	0.743	0.750

Polyethylene	45 mA	90 mA	180 mA	270 mA	350 mA
FBP	0.674	0.670	0.664	0.674	0.664
AIDR 3D	0.618	0.648	0.656	0.672	0.668
FIRST Body	0.631	0.680	0.689	0.700	0.688
FIRST Body Sharp	0.650	0.710	0.743	0.773	0.768

Acrylic	45 mA	90 mA	180 mA	270 mA	350 mA
FBP	0.752	0.729	0.723	0.726	0.731
AIDR 3D	0.680	0.696	0.714	0.725	0.735
FIRST Body	0.708	0.745	0.759	0.766	0.764
FIRST Body Sharp	0.727	0.762	0.804	0.823	0.827

Bone	45 mA	90 mA	180 mA	270 mA	350 mA
FBP	0.738	0.741	0.741	0.736	0.732
AIDR 3D	0.695	0.735	0.741	0.736	0.731
FIRST Body	0.917	0.906	0.901	0.903	0.897
FIRST Body Sharp	0.918	0.909	0.905	0.904	0.899

Table A2: Limiting spatial frequency (f_{10}) for each reconstruction algorithm and dose level.